



Perovskite/Ruddlesden-Popper composite fuel electrode of strontium-praseodymium-manganese oxide for solid oxide cells: An alternative candidate

Yousef Alizad Farzin^{a,b,*}, Mogens Bjerg Mogensen^a, Stéven Pirou^{a,1}, Henrik Lund Frandsen^a

^a Department of Energy Conversion and Storage, Technical University of Denmark, Lyngby Campus, 2800, Kgs. Lyngby, Denmark

^b Institute for Applied Materials - Electrochemical Technologies (IAM-ET), Karlsruhe Institute of Technology (KIT), Adenauerring 20b, 76131, Karlsruhe, Germany

HIGHLIGHTS

- The electrochemical performance studied in H₂ with 3–50 vol% H₂O.
- The SPM electrode presents a high electrocatalytic activity for steam electrolysis.
- The Rietveld refinement shows forming Ruddlesden-Popper phase in reducing gas.
- The perovskite to Ruddlesden-Popper transformation increases ionic conductivity.

ARTICLE INFO

Keywords:

Perovskite
Ruddlesden-Popper
SrPrMnO_{4+δ}
Electrolysis
Rietveld refinement
Electrochemical performance

ABSTRACT

Ni migrates from cermet fuel electrodes in SOECs at high overpotentials, prompting interest in alternative electrode materials. Ni-free perovskites with mixed ionic and electronic conductivity are being developed as substitutes for Ni-YSZ- or Ni-CGO-cermet fuel electrodes. However, some perovskite electrodes exhibit poor electrocatalytic activity during steam electrolysis. This study focuses on the synthesis, phase evolution, and cation oxidation state of Sr_{0.5}Pr_{0.5}MnO₃ (SPM) perovskite under oxidizing and reducing atmospheres. The electrochemical performance of the SPM electrode is investigated at different steam concentrations (3–50% H₂O in H₂). Rietveld refinement reveals a phase transformation from Pm-3m (221) to I4/mmm (139) in humidified 5% H₂ in N₂ gas at 800 °C. XPS measurements indicate that the I4/mmm (139) structure contains more oxygen vacancies, enhancing ionic conductivity and electrocatalytic activity. At 610 °C, the SPM electrode with the Pm-3m (221) space group exhibits a low polarization resistance of 0.173 Ω cm² in 50% H₂O in H₂ gas. However, forming a Ruddlesden-Popper structure increases polarization resistance at higher temperatures due to a low-frequency reaction. Overall, the SPM electrode shows promising electrocatalytic activity across a wide range of oxygen partial pressure, making it a potential fuel electrode in SOECs.

1. Introduction

Solid oxide cells (SOCs) have gained significant attention as one of the most efficient and environmentally friendly methods of converting chemical energy into electricity in fuel cell mode as well as producing H₂, CO, or a mixture of them from H₂O and CO₂ in electrolysis mode [1, 2]. Using solid oxide electrolysis cells (SOECs) at high temperatures produces hydrogen with a lower electricity cost than low-temperature electrolysis, as the thermodynamics at high temperatures are more

favorable [1]. The nickel-yttrium stabilized zirconia (Ni-YSZ) with excellent electrochemical performance are widely used as the fuel electrode in solid oxide fuel cells (SOFCs). Due to its excellent electrical conductivity, catalytic activity, and high-temperature stability, this electrode is also a candidate for SOECs. However, the electrochemical performance of this Ni-based composite electrode may degrade fast at high overpotential due to the Ni migration out of electrocatalytic active sites. This problem encourages the development of alternative materials for fuel electrodes.

* Corresponding author. Department of Energy Conversion and Storage, Technical University of Denmark, Lyngby Campus, 2800, Kgs. Lyngby, Denmark.
E-mail address: yousef.farzin@kit.edu (Y. Alizad Farzin).

¹ Current address: Topsoe A/S, Haldor Topsøes Allé 1, 2800 Kgs. Lyngby, Denmark.

Replacing YSZ with gadolinia-doped ceria (CGO) has been extensively studied as a solution to overcome Ni-YSZ limitations in SOCs operating at intermediate temperatures (500–750 °C) [3,4]. CGO with a fluorite structure enhances the catalytic activity of Ni-GDC electrodes in fuel oxidation and H₂O electrolysis by extending the three-phase boundary (3PB) to the entire electrode surface [5]. This extension of the active site area may help address the Ni migration problem in Ni-YSZ electrodes. However, the Ni migration issue worsens in the early stages of operation (before 1000 h) at higher current densities ($> -1 \text{ A cm}^{-2}$) [6,7]. This problem persists even at low current densities (-0.5 A cm^{-2}) after long-term operation (100,000 h at 700 °C) in fuel cell mode [8]. The degradation of the electrode is a complex process involving the evolution of both Ni and GDC phases, which is influenced by humidity and steam concentration.

Sciazko et al. [9], investigated the degradation rate and micro-structural evolution of Ni-GDC and Ni-YSZ electrodes in SOEC and SOFC modes. While Ni-GDC electrodes initially performed better due to extended reaction sites, Ni-YSZ electrodes exhibited greater stability throughout the operation period. The higher degradation rate of Ni-GDC electrodes can be attributed to interactions between Ni and GDC particles, forming a GDC layer on Ni grains. Coarsening of Ni particles and depletion of Ni from the electrolyte were observed regardless of the active site configuration. In SOEC operation, the YSZ formed a stable backbone while GDC covered the Ni grains in the Ni-YSZ electrode. Vibhu et al. [10] investigated the addition of small quantities of gold or molybdenum to improve the electrocatalytic activity of Ni-GDC electrodes and suppress Ni migration during high-temperature electrolysis. The modified Ni-GDC electrode showed a maximum current density of -0.78 A cm^{-2} at 900 °C with certain metal additives, but the mitigation of Ni migration phenomena was not significant after extended operation.

Using mixed ionic-electronic conductors (MIECs) will also extend the active electrochemical sites from the 3PB to the entire electrode surface (two-phase boundary, 2PB) towards the gas reactant. It can effectively decrease the polarization resistance (R_p) in the SOCs. The perovskites are the most common MIECs materials studied as the oxygen and fuel electrodes [11–15]. When used as a fuel electrode, some perovskites have high chemical stability due to relatively stable-oxidation state cations like Ti, V, and Cr at the B sites. For instance, the structural stability of the $\text{La}_{0.75}\text{Sr}_{0.25}\text{Cr}_{0.5}\text{Mn}_{0.5}\text{O}_3$ [16], $\text{La}_{0.6}\text{Sr}_{0.4}\text{VO}_3$ [17], and $\text{Sr}_{0.94}\text{Ti}_{0.9}\text{Nb}_{0.1}\text{O}_3$ [18] in reducing atmosphere make them suitable backbone for the fuel electrode. However, the insufficient catalytic activity and oxide ion conductivity cause poor electrochemical performance in these electrodes.

Generally, it can be stated that the cations in the B-sites primarily ensure the catalytic performance of the perovskites, and A-site cations stabilize the structure [19]. Among the developed electrode materials, Mn-based perovskites have attracted much attention due to their high electrocatalytic activity [20]. Mn cations with three oxidation states, i. e., $\text{Mn}^{4+}/\text{Mn}^{3+}/\text{Mn}^{2+}$, provide an increased capability to optimize catalytic activity and mixed-ionic and electronic conductivity. Partly substituting Sr cations at A-sites in LaMnO_3 can enhance oxidation activity, which is associated with increasing Mn^{4+} concentration in the perovskite structure [21–23]. Even though the A-site cations are not directly involved in the catalytic process, a good combination of these cations can enhance the number of Mn^{4+} ions for better electrochemical performance.

Another approach for improving the catalytic activity of fuel electrodes is to incorporate nanosized catalyst particles of compositions such as Pd, Ni, and $\text{Ce}_{0.9}\text{Gd}_{0.1}\text{O}_{2.8}$ (CGO) into perovskite oxides. Therefore, impregnating or infiltrating the solution is a successful way to construct active electrodes [24]. Despite the considerable improvement of the electrode performance, the electrochemical activity highly depends on the uniformity and the morphology of catalysts on the electrode surface [25]. In addition, the chemical interaction between the backbone and the decorating particles may affect the catalyst functionality over the

long-term operation. For these reasons, many studies have focused on developing an easy method to create more uniformly distributed and firmly attached nanoparticles to the electrode backbone.

Using cation exsolution from the B-sites of the perovskite structure provides an alternative approach to uniformly coating the electrode structure with smaller and well-adhered particles [13]. Recent studies on the electrochemical performance of the perovskites showed that transition metals such as Ni, Co, Mn, and Fe could be exsolved under fuel electrode operating conditions to produce nanoparticles catalyst [26, 27]. Thus, metallic nanoparticles with excellent activity and stability improved the electrochemical performance of the fuel electrodes [25, 28]. Besides the cost-effectiveness of this method, it is less affected by other factors, such as the morphology of the electrode backbone, the viscosity of the infiltration solution, and the chemical compatibility of electrode materials and the infiltrated nanoparticles [29].

Sengodan et al. [30] have studied the in situ exsolution of Mn cations for $\text{NdBaMn}_2\text{O}_{5+\delta}$ (NBMO) perovskite. The atomic-resolved high-angle annular dark field (HAADF) scanning transmission electron microscopy (STEM) images illustrated that the electrode backbone was decorated with the nanoparticles when it was reduced under pure hydrogen at 800 °C, and energy-dispersive X-ray spectroscopy (EDX) point analysis identified them as the cubic MnO phase. Furthermore, Gibbs' free energy for the reduction (ΔG_{red}) of Mn oxide under pure hydrogen at 900 °C provides further proof of the stability of MnO [31]. The ΔG_{red} for reducing MnO to metallic Mn is greater than 100 kJ mol^{-1} [32]. The electrocatalytic activity of MnO improved the electrochemical performance of the NBMO fuel electrode at 800 °C, and despite using thick yttria-stabilized zirconia (YSZ) electrolyte (120 μm), a high power density of 580 mW cm^{-2} was achieved in 3% H₂O in H₂ with using $\text{La}_{0.8}\text{Sr}_{0.2}\text{FeO}_3$ (LSF) as the oxygen electrode.

The studies of the exsolution of cations have primarily focused on how it affects electrochemical performance. Still, the phase composition of the backbone and the oxygen vacancy concentration should play a significant role in determining the total polarization resistance. The final chemical composition of electrode material under working conditions highly depends on the initial composition. For example, the $\text{Ln}_{1-x}\text{Ba}_x\text{MnO}_{3-\delta}$ (Ln = La and Pr) with perovskite structure transforms to $\text{A}_2\text{Mn}_2\text{O}_5$ layered perovskite upon heat treatment in reducing conditions [33,34], while replacing the Ba with Sr leads to forming A_2MnO_4 Ruddlesden-Popper (RP, $\text{A}_{n+1}\text{B}_n\text{O}_{3n+1}$ n=1) structure rather than $\text{A}_2\text{Mn}_2\text{O}_5$ layered perovskite (Brownmillerite) [35]. Previous studies on both $\text{A}_2\text{Mn}_2\text{O}_5$ and A_2MnO_4 structures have shown the capacity to contain a high concentration of oxygen vacancies after these phase transformations [34,36]. It is proposed that the high activity of these materials originates from increased oxygen vacancy concentration and improved redox properties [37].

The formation of a conductive backbone coupled with the exsolution of nanocatalysts makes it possible to achieve superior electrocatalytic activity. This paper investigates the electrochemical performance of the $\text{Sr}_{0.5}\text{Pr}_{0.5}\text{MnO}_3$ (SPM) perovskite in a wide range of oxygen partial pressures ($p\text{O}_2$) for the first time. The partial phase transformation of SPM perovskite to Ruddlesden-Popper structure could provide an opportunity to form a composite electrode in situ. The ionic conductivity can be accelerated by forming the RP phase, and catalytic activity can be enhanced on the surface of the reduced perovskite. Meanwhile, the exsolution of MnO catalyst particles could further improve the surface reactions to achieve superior performance. Our focus is to study the effect of gas composition on the unit cell structure, electrical conductivity, and oxidation state of the cations as the determining parameters in the final electrochemical performance. Rietveld refinement was performed on heat-treated powder in the air and humidified 5% H₂ in N₂ atmospheres to determine structural space group and phase purity. Using the Van Der Pauw four-point method, the electrical conductivity of SPM was measured, and the valence state of the cations on its semi-conducting behavior was investigated. Last but not least, the electrochemical properties of prepared SOCs were examined in H₂ with a wide

range of steam concentrations.

In order to better understand the variation in polarization resistances and superior electrochemical performance achieved by the RP structure at a low temperature, we have first discussed phase evolution, the oxidation state of cations, and other phenomena occurring under working conditions. Thus, it can provide good insight into the evolution of crystal structure properties as a function of pO_2 and allow a deeper understanding of the electrocatalytic activity of the developed fuel electrode.

2. Experimental

2.1. Preparation process

The $Sr_{0.5}Pr_{0.5}MnO_3$ (SPM) perovskite powder was synthesized via the sol-gel combustion method. Accordingly, the stoichiometric amount of $Pr(NO_3)_3 \cdot 6H_2O$, $Sr(NO_3)_2$, and $Mn(NO_3)_2 \cdot 4H_2O$ were dissolved together in citric acid ($C_6H_8O_7$) with a molar ratio of 1:1.5 (metal nitrates: citric acid). The dissolved precursor was stirred for 3 h at 70 °C to achieve a transparent aqueous solution. The pH was adjusted to about 7 by adding an ammonia solution. Then, the obtained sol was kept at 70 °C overnight to vaporize the water and form a viscous gel. The produced gel was heat-treated at 350 °C (for 1 h, with a heating rate of 300 °C/h) to form black ash. As a result of the redox reactions, nitrates and carboxyl groups acted as oxidants and reductants, respectively, to produce simple oxides [38,39]. The ash was transferred from the glass beaker to the alumina crucible and heat-treated at 800 °C (for 3 h, with a heating rate of 180 °C/h) in the air to burn out the residual organic components. Finally, the resulting powder was heat-treated at 1000 °C in an N_2 atmosphere to form SPM perovskite (for 3 h, with a heating rate of 180 °C/h). The pO_2 in the N_2 atmosphere was determined to be 6.37×10^{-7} atm. Moreover, final heat treatment was conducted in humidified 5% H_2 in N_2 (2.9% H_2O - 4.9% H_2 - 92.2% N_2) gas to investigate the phase evolution in a reducing atmosphere. The pO_2 for this gas at 600, 650, 700, 750, and 800 °C was measured to 4.71×10^{-25} , 1.88×10^{-23} , 5.17×10^{-22} , 1.03×10^{-20} , and 1.56×10^{-19} atm, respectively.

To prevent electronic conduction through the electrolyte, a thin $(ZrO_2)_{0.89}(Sc_2O_3)_{0.1}(Y_2O_3)_{0.01}$ (10Sc1YSZ) layer is sandwiched between two thick $Ce_{0.9}Gd_{0.1}O_2$ (CGO) layers. The CGO and 10Sc1YSZ tapes were prepared by tape-casting using a doctor blade gap of 500 μm and 80 μm , respectively. They were then laminated via a double roll setup heated at 120 °C using a speed of 45 cm/min and were then sintered for 6 h at 1300 °C. The slow heating rate of 20 °C/h was set from room temperature to 550 °C to facilitate gas diffusion during the decomposition of the binders. The sintered thicknesses for the CGO and 10Sc1YSZ layers correspond to 70 μm and 7 μm , respectively. The thick CGO layers primarily support the thin 10Sc1YSZ layer, allowing the cell to be handled easily for electrochemical testing. In other words, this approach facilitates the preparation of mechanically robust cells with high conductivity of oxide ions through the electrolyte while keeping the processing simple. Typically, the supporting layer in a commercial cell is made of strong materials, such as zirconia for the electrolyte and electrode-supported cells or stainless steel for metal-supported cells. By this approach, it will be possible to reduce the thickness of the CGO layer to a few microns with the only purpose of inhibiting chemical reactions at the electrode and zirconia-based electrolyte interfaces. However, the processing of such a cell is more complex due to the co-sintering of the many layers, which has been avoided in the research here by applying the electrodes through screen printing.

The SPM ink for screen printing was prepared by mixing the ceramic powder and additives. The ink was then applied to both electrode sides by screen-printing (EKRA-E2, Germany). The precursors were mixed for 5 h at 200 rpm in a planetary ball mill (RETSCH-PM 400) with the aid of zirconia cups and balls. Dipropylenglycol (DPG), poly(methylmethacrylate) (PMMA), sanitizer 261A, polyvinylpyrrolidone (PVP) K30, and PVP K90 were used as the solvent, pore former, plasticizer,

dispersant, and binder, respectively. As a prerequisite for obtaining a crack-free electrode after the sintering process, it is necessary to use a slow heating rate of 20 °C/h at temperatures ranging from 25 to 550 °C to allow gas diffusion during the decomposition of the binders. Finally, the sintering process of the symmetric solid oxide cell was followed by heat treatment at 1200 °C for 4 h in the air, with a ramp rate of 60 °C/h from 550 °C.

2.2. Characterization

The phase evolution in SPM perovskite was studied with X-ray diffraction at room temperature in the 2θ range of 10–90° using a Rigaku MiniFlex 600 diffractometer with $CuK\alpha$ radiation ($k = 1.5418 \text{ \AA}$). The Rietveld refinement was performed on powders heat-treated in nitrogen and 3% H_2O + 5% H_2 in N_2 gases using MATCH software to identify space groups, lattice parameters, and quantitative analysis. An analysis of the oxidation state of cations in the prepared samples was carried out by XPS (Thermo Scientific, ESCALAB XI⁺) using an Al $K\alpha$ radiation monochromatic source. The microstructure of the sintered electrode was studied with a field emission scanning electron microscope (Zeiss-Merlin FE-SEM) and an energy-dispersive spectrometer (Bruker XFlash 6160).

The electrical conductivity of the SPM electrode was investigated using the four-point Van der Pauw method. The measurement was conducted under air and humidified 5% H_2 in N_2 gas from room temperature to 800 °C. The heating and cooling rates were set to 20 °C h^{-1} to record the electrical conductivity near the equilibrium conditions. Besides, the sample was kept for 5 h at 800 °C to study the effect of dwell time on electrical conductivity. The measurement continued with cooling the sample to room temperature with a similar slow cooling rate to study the reversibility of phenomena during the heating cycle. The electrochemical performance was studied using a 1260 Solarton frequency response analyzer under different gases at 610–760 °C, and the obtained results were fitted via the Zview software. The applied frequency ranged from 10 mHz to 1 MHz with a voltage amplitude of 3 mV.

The impedance measurement was repeated three times on samples from the same batch to determine the reproducibility of the data. Accordingly, the measurement was initiated in the gas with the highest pO_2 (50% H_2O in H_2) at different temperatures and then switched to other gas compositions. It is important to note that testing the samples under the mentioned protocol had no detrimental effect on the performance of the cells before exposure to the subsequent gas compositions.

3. Results and discussion

3.1. Phase evolution

Fig. 1 shows the X-ray diffraction pattern of the synthesized powder at different temperatures and gas compositions. Inorganic crystal structure database (ICSD) reference cards were used to identify the phase composition in the prepared sample. The formed ash in the sol-gel combustion method was heat-treated at 800 °C to burn out the residual organic components [40,41]. Subsequently, the SPM perovskite was formed with heat treatment at 1000 °C in N_2 gas (Fig. 1a). The pO_2 of the N_2 atmosphere was 6.37×10^{-7} atm as measured by a sensor installed in the furnace tube. The observed peaks match the ICSD #187094 reference card without impurity phases. The obtained powder is further heat-treated in humidified 5% H_2 in N_2 gas at 600 to 800 °C to study the phase evolution during conditions corresponding to the cell operation (Fig. 1b, c, and d). Here pO_2 of the utilized gas at 600, 650, 700, 750, and 800 °C measured at 4.71×10^{-25} , 1.88×10^{-23} , 5.17×10^{-22} , 1.03×10^{-20} , and 1.56×10^{-19} atm, respectively.

XRD pattern in Fig. 1b indicates that no phase transformation occurred after heat treatment at 600 °C in humidified 5% H_2 in N_2 , and only perovskite was observed. However, increasing the heat treatment temperature to 700 °C (Fig. 1c) leads to a perovskite (ICSD #187094) to Ruddlesden-Popper (ICSD #98363) phase transformation. The general

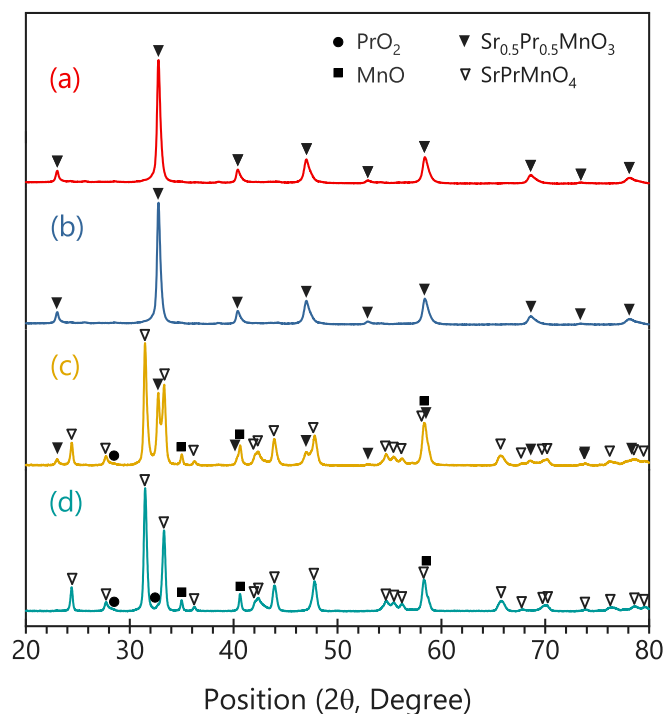


Fig. 1. X-ray diffraction pattern of SPM powder after heat treatment at (a) 1000 °C in N₂ atmosphere, and then reduced powder in humidified 5% H₂ in N₂ gas at (b) 600, (c) 700, and (d) 800 °C.

formula for the RP structure is A_{n+1}B_nO_{3n+1} (n = 1, 2, 3, ...), in which the phase with n = 1 (A₂BO₄, SrPrMnO_{4+δ}) is formed in this study. The quantitative calculation showed that about 63 wt% of SPM perovskite transformed to Ruddlesden-Popper at 700 °C. Comparing the crystal structure for Sr_{0.5}Pr_{0.5}MnO₃ perovskite and SrPrMnO_{4+δ} Ruddlesden-Popper shows that the Sr, Pr, and Mn cations occupy similar octahedral and dodecahedral sites in these structures. In contrast, the arrangement of the cations layers and the number of oxygen ions in the molecule formula changes with phase transformation. Further details about the crystal structure and occupancy of crystal sites are discussed in the Rietveld refinement section.

The phase evolution study was completed by further increasing the heat treatment temperature to 800 °C. Meanwhile, changing the oxidation state of Mn and Pr cations in a reducing atmosphere led to the formation of MnO (ICSD #76086) and PrO₂ (ICSD #105541) phases. The identified phases at this temperature consisted of 85.1 wt% SrPrMnO_{4+δ}, 14.2 wt% MnO, and 0.7 wt% PrO₂. It is worth mentioning that after forming the Ruddlesden-Popper structure at 800 °C, it had a stable structure in a humidified 5% H₂ in N₂ atmosphere over the temperature range of 600–800 °C. In addition, the XRD results showed the reversibility of Ruddlesden-Popper to perovskite transformation when it was heat-treated again in the N₂ at 1000 °C (see [supplementary information Fig. 1s](#)).

As a result of the perovskite reduction, the phase transformation reaction is proposed to occur as follows [42].



This phase transformation is recognized as the reconstruction of cations in the perovskite and the formation of a Ruddlesden-Popper structure, while the B-site cations are exsolved onto the backbond particles. However, the B-site exsolution requires an A-site deficiency to increase the coefficient of cation diffusion to the surface; otherwise, the segregation within the bulk would be the preferred mechanism. Although several perovskites have demonstrated a superior distribution of catalyst particles on their surfaces when they undergo phase transformation into RP

[43], the mechanism of phase reconstruction and the amount of exsolved cations are still open questions. X-ray diffraction patterns indicate both the exsolution of MnO and the formation of a minor A-site deficiency due to the formation of PrO₂ in the reduced perovskite. Unlike other Ni, Fe, and Co-containing perovskites that form metallic particles on the surface of perovskites [44–47], the Mn cations remain in oxide form after exsolution in this work. The same behavior has been observed for Nb_{0.5}Ba_{0.5}MnO_{3-δ} perovskite when exposed to a reducing atmosphere with oxygen partial pressure of 10⁻²⁵ to 10⁻² atm [30].

An additional analysis of the XRD pattern for prepared samples was conducted using the Rietveld refinement method (Fig. 2). The details of refined parameters, i.e., the space group, lattice parameters, and site occupancy, are summarized in Table 1, where the R_{WPattern} (R-weighted-pattern), R_{Pattern} (R-pattern), and χ² values indicate that the refinement results are reasonable. The excellent agreement between the diffraction pattern and the refined profiles indicates good cation ordering between Pr/Sr and Mn cations in the SPM lattice structure. The Rietveld analysis of the XRD pattern for SPM perovskite reveals a cubic structure with a Pm-3m (221) space group, and the calculated lattice parameter is 3.8649 Å.

The heat treatment of SPM perovskite in reducing conditions forms oxygen vacancies in the crystal structure, and decreasing the oxygen content coincides with an increase in lattice volume [48]. Accordingly, the refined parameters for heat-treated powder in a humidified 5% H₂ in N₂ atmosphere reveal a substantial increase in c = 12.8046 Å, while other lattice parameters remain at the same order of magnitude, a = b = 3.79799 Å. The calculated values are very close to the lattice parameters of La_{0.5}Sr_{1.5}MnO_{4+δ} [35] with a Ruddlesden-Popper structure. One of the significant factors limiting the electrocatalytic properties of perovskites in SOCs applications is the formation of an isolating component at high steam concentrations. For instance, forming SrMoO₄ in high pO₂ causes a drastic increase in polarization resistance in Sr₂FeMoO₆ perovskite [11].

The capability of the SPM perovskite to change its crystal structure in response to pO₂ could mitigate the formation of a secondary phase under cell operation conditions. However, the variation of lattice parameters in the reducing atmosphere leads to an expansion in unit cell volume. The unit cell volumes for the perovskite and Ruddlesden-Popper are calculated at 57.73 and 184.70 Å³, respectively. According to Fig. 2, the Ruddlesden-Popper (RP) structure consists of a perovskite layer (P) sandwiched between two rock-salt layers (RS). The ideal perovskite structure contains five ions, while an ideal Ruddlesden-Popper structure contains fourteen ions. The presence of crystal defects such as vacancies, substitutional, and interstitial defects causes a deviation from the ideal number of ions in these structures. It is reported that oxygen vacancies are found in the perovskite layer, and interstitial oxygen is located in the rock-salt layers of the RP structure [49]. To the best of our knowledge, the substitutional and interstitial defects have not been reported for the A and B sites in the P and RP structures, whereas the cations vacancies can be formed during the synthesis and phase transformation in this study.

The volume expansion percentage can be calculated by using the number of ions in the unit cell and the volume of the unit cell in the following equation.

$$\Delta V(\%) = \frac{V_{RP} - \frac{n_{RP}}{n_P} V_P}{V_{RP}} \times 100 \quad (2)$$

V is the unit cell's volume, and n is the number of ions in the unit cell for the P and RP structures. Based on the obtained site occupancies from the Rietveld refined in Table 1, the mean number of ions in the P and RP unit cells are calculated at 4.62 and 14.74, respectively. Therefore, the transformation of perovskite to Ruddlesden-Popper leads to a 0.28% expansion of the crystal volume. It is necessary to mention that the average coefficient of thermal expansion (CTE) for a similar oxide with the chemical composition of Pr_{0.65}Sr_{0.3}MnO_{3-x} measured in the air was

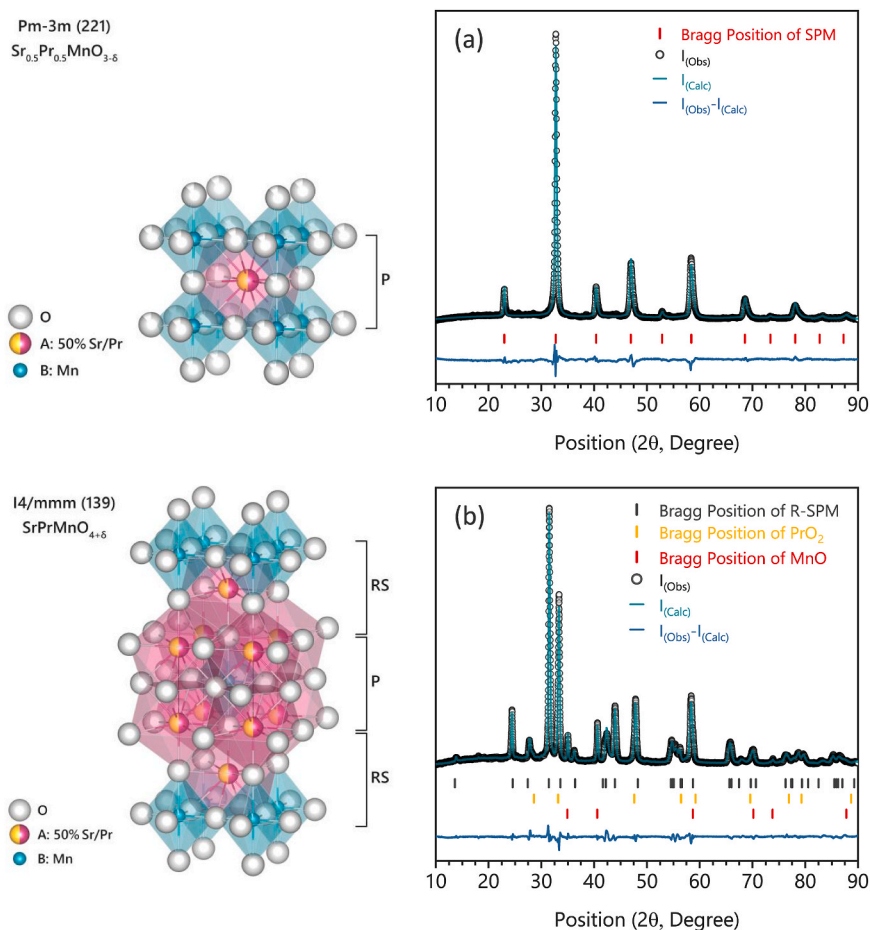


Fig. 2. Rietveld refinement profile of (a) SPM and (b) reduced SPM powder. The SPM perovskite was heat treated in N_2 at $1000\text{ }^\circ\text{C}$ and reduced powder with Ruddlesden-Popper structure heat treated in humidified $5\% H_2$ in N_2 gas. The pO_2 of these two oxidizing and reducing conditions is 6.37×10^{-7} atm and 1.56×10^{-19} atm, respectively. I_{Obs} and I_{Calc} show the obtained result from equipment and the calculated profile by Rietveld refinement, respectively.

Table 1

The Rietveld refinement parameters and structural details for the SPM perovskite and reduced SPM powder with Ruddlesden-Popper structure. The pO_2 of heat treatment conditions to synthesize the SPM perovskite in N_2 and reduced SPM powder in humidified $5\% H_2$ in N_2 gas is 6.37×10^{-7} atm and 1.56×10^{-19} atm, respectively.

| Sample | SPM perovskite | Reduced SPM powder | | |
|-----------------------|-----------------------------|--------------------|-------------|-------------|
| $R_{Pattern}$ (%) | 6.37 | 3.45 | | |
| $R_{WPattern}$ (%) | 7.73 | 4.49 | | |
| χ^2 | 8.51 | 2.61 | | |
| Number of phases | 1 | 3 | | |
| Phase | $Sr_{0.5}Pr_{0.5}MnO_{3.6}$ | $SrPrMnO_{4.6}$ | MnO | PrO_2 |
| ICSD reference card | 187094 | 98363 | 76086 | 105541 |
| Space group | Pm-3m (221) | I4/mmm (139) | Fm-3m (225) | Fm-3m (225) |
| Quantity (wt.%) | 100 | 85.1 | 14.2 | 0.7 |
| α ($^\circ$) | 90.000 | 90.000 | 90.000 | 90.000 |
| β ($^\circ$) | 90.000 | 90.000 | 90.000 | 90.000 |
| γ ($^\circ$) | 90.000 | 90.000 | 90.000 | 90.000 |
| a (\AA) | 3.8649 | 3.79799 | 4.43378 | 5.42389 |
| b (\AA) | – | – | – | – |
| c (\AA) | – | 12.8046 | – | – |
| V (\AA^3) | 57.732 | 184.703 | 87.161 | 159.563 |
| Element (1) | Sr | Sr | Mn | Pr |
| Occupancy (1) | 0.4996 | 0.4927 | 1.0000 | 1.3666 |
| Element (2) | Pr | Pr | O | O |
| Occupancy (2) | 0.4977 | 0.5072 | 0.9407 | 1.0000 |
| Element (3) | Mn | Mn | | |
| Occupancy (3) | 0.9999 | 0.9805 | | |
| Element (4) | O | O | | |
| Occupancy (4) | 0.8747 | 1.0938 | | |
| Element (5) | | O | | |
| Occupancy (5) | | 1.1022 | | |

reported at $11.6 \times 10^{-6} \text{ K}^{-1}$ for the temperature range of 30–1000 °C [50], which is close to the corresponding value for the YSZ electrolyte ($11 \times 10^{-6} \text{ K}^{-1}$) [51]. The crystal expansion is calculated for the heat-treated powder under $p\text{O}_2$ of $1.56 \times 10^{-19} \text{ atm}$. A similar expansion order is also expected for the electrode operated at open circuit voltage (OCV) using 50% $\text{H}_2\text{O}/\text{H}_2$ at 800 °C, which gives the same $p\text{O}_2$ of 4.46×10^{-19} . The 0.28% expansion of the electrode falls within an acceptable range for operating the cell without experiencing failure. However, sintering the electrode under a reducing atmosphere can be implemented as a practical approach to avoid interfacial stress at the electrode/electrolyte interface.

3.2. XPS analysis

The oxidation state of the cations plays an important role in evaluating ionic and electronic conductivity, which in turn affects the final electrochemical performance. Fig. 3 shows the deconvolution of XPS spectra of Sr 3d, Pr 3d, Mn 2p, and O 1s for the SPM oxide with perovskite and Ruddlesden-Popper structure. The constrained peaks with equal full width at half maximum (FWHM) and constant area ratio based on the orbital electron were used to fit the cations spectra [52]. The details of fitted curves are summarized in Table 2.

In general, the electrocatalytic activity of perovskites is primarily determined by the cations on their B sites [19,53]. Although the cations in the A sites are not involved in the catalytic reaction, A-site substitution or deficiency can also regulate the catalytic activity due to the charge compensating of the cations in B sites. Another factor affecting electrocatalysis is the tendency of Sr ions to segregate on the electrode surface and form SrO compounds with poor catalytic activity [54].

Fig. 3a₁ and Fig. 3a₂ show the core-shell level spectra of the Sr 3d for the heat-treated powder in N_2 and humidified 5% H_2 in N_2 , respectively. Spectra of Sr 3d were deconvoluted into surface and lattice components to provide insight into the number of surface species and their evolution under different heat treatment atmospheres, in which the Sr surface species (SSS), i.e., surface oxide, hydroxide, carbonate or sulfate, identify with the peaks at high binding energies [55–57]. As a requirement for accurate analysis of the XPS spectra, the area ratio between fitted peaks for the $3d_{3/2}$ and $3d_{5/2}$ levels was restricted to 2/3 according to the number of electrons on each level, and the FWHM being set to identical for each pair of components.

For the sample heat-treated in the N_2 atmosphere (Fig. 3a₁), lattice component peaks are located at 132.21 eV and 134.01 eV for $3d_{3/2}$ and $3d_{5/2}$ orbitals, respectively, and are correlated with the corresponding positions for perovskites [56]. The second heat treatment of the powder

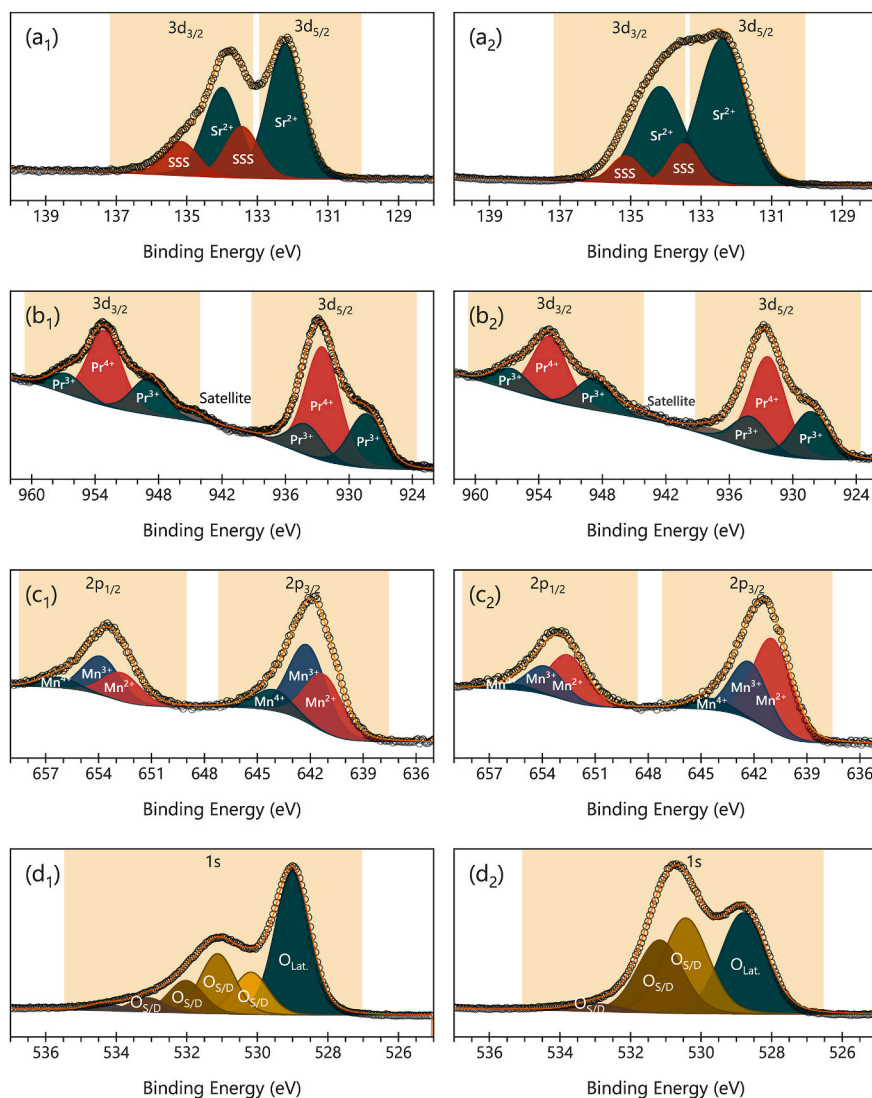


Fig. 3. The core-level spectra of (a) Sr 3d, (b) Pr 3d, (c) Mn 2p, (d) O 1s for SPM powder. The spectra with numbers 1 and 2 represent the results obtained for heat-treated powder at 1000 °C in N_2 with perovskite structure and heat-treated powder at 800 °C in 3% H_2O + 5% H_2 in N_2 with Ruddlesden-Popper structure, respectively.

Table 2

The binding energies, FWHM, peak area, and percentage contributions of core electrons for Sr 3d, Pr 3d, Mn 2p, and O 1s for SPM double perovskite.

| Atmosphere | Spin State | Oxidation State | Binding Energy (eV) | FWHM (eV) | Concentration (at. %) |
|---|------------|------------------------|---------------------|-----------|-----------------------|
| N ₂ | 3d5/2 | Sr ²⁺ | 132.21 | 1.19 | 43.93 |
| | | SSS | 133.43 | 1.14 | 16.07 |
| | 3d3/2 | Sr ²⁺ | 134.01 | 1.19 | 29.29 |
| | | SSS | 135.17 | 1.14 | 10.71 |
| | 3d5/2 | Pr ³⁺ | 928.38 | 3.82 | 16.41 |
| | | Pr ⁴⁺ | 932.51 | 3.82 | 34.16 |
| | 3d3/2 | Pr ³⁺ | 934.06 | 3.82 | 9.43 |
| | | Pr ³⁺ | 948.92 | 3.82 | 10.94 |
| | | Pr ⁴⁺ | 953.08 | 3.82 | 22.78 |
| | | Pr ³⁺ | 956.59 | 3.82 | 6.29 |
| | 3p3/2 | Mn ²⁺ | 641.23 | 2.53 | 24.41 |
| | | Mn ³⁺ | 642.15 | 2.53 | 33.10 |
| | | Mn ⁴⁺ | 644.07 | 2.53 | 9.15 |
| | 3p1/2 | Mn ²⁺ | 652.68 | 2.53 | 12.21 |
| | | Mn ³⁺ | 653.85 | 2.53 | 16.55 |
| | | Mn ⁴⁺ | 656.23 | 2.53 | 4.58 |
| | 1s | O ²⁺ (Lat.) | 529.00 | 1.17 | 48.83 |
| | | O ²⁺ (S/D.) | 530.18 | 1.17 | 14.45 |
| | | O ²⁺ (S/D.) | 531.12 | 1.17 | 20.52 |
| | | O ²⁺ (S/D.) | 532.02 | 1.17 | 11.19 |
| O ²⁺ (S/D.) | | 533.10 | 1.17 | 5.01 | |
| 3% H ₂ O + 5% H ₂ in N ₂ | 3d5/2 | Sr ²⁺ | 132.40 | 1.59 | 50.83 |
| | | SSS | 133.49 | 1.01 | 9.17 |
| | 3d3/2 | Sr ²⁺ | 134.16 | 1.59 | 33.89 |
| | | SSS | 135.15 | 1.01 | 6.11 |
| | 3d5/2 | Pr ³⁺ | 928.29 | 3.96 | 16.08 |
| | | Pr ⁴⁺ | 932.35 | 3.96 | 32.73 |
| | 3d3/2 | Pr ³⁺ | 933.97 | 3.96 | 11.19 |
| | | Pr ³⁺ | 948.75 | 3.96 | 10.72 |
| | | Pr ⁴⁺ | 952.97 | 3.96 | 21.82 |
| | | Pr ³⁺ | 956.52 | 3.96 | 7.47 |
| | 3p3/2 | Mn ²⁺ | 640.94 | 2.55 | 38.09 |
| | | Mn ³⁺ | 642.25 | 2.55 | 23.75 |
| | | Mn ⁴⁺ | 644.32 | 2.55 | 4.83 |
| | 3p1/2 | Mn ²⁺ | 652.53 | 2.55 | 19.05 |
| | | Mn ³⁺ | 653.81 | 2.55 | 11.87 |
| | | Mn ⁴⁺ | 655.59 | 2.55 | 2.42 |
| | 1s | O ²⁺ (Lat.) | 528.80 | 1.53 | 36.40 |
| | | O ²⁺ (S/D.) | 530.43 | 1.53 | 34.33 |
| | | O ²⁺ (S/D.) | 531.17 | 1.53 | 26.30 |
| | | O ²⁺ (S/D.) | 532.92 | 1.53 | 2.98 |

in humidified 5% H₂ in N₂ gas leads to a small shift (0.15–0.2 eV) to the higher binding energy, which is mainly due to phase transformation from perovskite to Ruddlesden-Popper structure.

Meanwhile, identifying almost identical peak positions for the corresponding peaks to the Sr surface species show different behavior than the lattice component. The peak positions for the SSS components are located at 133.06 (±0.03) eV and 135.16 (±0.01) for 3d_{3/2} and 3d_{5/2} orbitals, respectively. Furthermore, the quantitative analysis indicates that after a second heat treatment in humidified 5% H₂ in N₂, the area ratio of SSS/Sr²⁺ peaks decreases from 0.37 to 0.18, which shows the diffusion of Sr surface species back to the Ruddlesden-Popper structure. Accordingly, decreasing the concentration of Sr oxide as an electrocatalytic passive component from the electrode surface could improve the electrocatalytic activity.

As mentioned earlier, the catalytic activity of the electrode material can be regulated by the influence of A-site ions on the valence state of cations in the B-sites. Therefore, a scan of Pr 3d spectra was performed to estimate the valence state of the praseodymium (Fig. 3 b₁). The scanned spectra were deconvoluted considering the area ratio of 2:3 for 3d_{3/2} to 3d_{5/2} levels. The fitted peak for Pr 3d spectra exhibits three peaks corresponding to the binding energy of Pr³⁺ and Pr⁴⁺ cations. The binding energy at 928.38 and 934.06 eV could be assigned to Pr³⁺ 3d_{5/2}, whereas the peak at 932.51 eV was ascribed to Pr⁴⁺ 3d_{5/2} [58,59]. The XPS spectra confirm the presence of a multivalence state in the Pr ions,

which could provide good electronic conductivity in the SPM structure. The area of fitted peaks for Pr³⁺ and Pr⁴⁺ shows a slight change with a phase transformation from perovskite to Ruddlesden-Popper, resulting in a minor increase in the Pr³⁺/Pr⁴⁺ ratio from 0.76 to 0.83. Accordingly, it can be concluded that the valence state of Pr in the SPM powder is not highly influenced by the heat treatment atmosphere, as seen in the similar average oxidation state of Pr on the surface of Sr_{0.5}Pr_{0.5}MnO₃ and SrPrMnO_{4+δ} (i.e., +3.57 and +3.55, respectively). It is worth mentioning that the presence of about 2 wt% of PrO₂ in the reduced sample slightly increases the average oxidation state for Pr cations; however, it has no significant effect on the calculated values.

The Mn 2p spectra display two peaks corresponding to the spin-orbital splitting of the Mn 2p_{3/2} and Mn 2p_{1/2} sub-levels (Fig. 3c₁ and Fig. 3c₂). The fitted peaks in Mn 2p_{3/2} demonstrate a nice fitting of three peaks centered at 641.23, 642.15, and 644.07 eV. It has previously been reported that these peaks were assigned to Mn²⁺, Mn³⁺, and Mn⁴⁺ cations, respectively [12,60]. The quantitative analysis in Table 2 shows the significant influence of the heat treatment atmosphere on the valence state of Mn ions in prepared samples. Reduction of SPM perovskite in humidified 5% H₂ in N₂ atmosphere increases the number of Mn²⁺ cations from 36.62 to 57.14 at.%. Consequently, the average oxidation state of Mn cations in SPM perovskite decreased from +2.77 to +2.50 in the Ruddlesden-Popper structure with the chemical formula SrPrMnO_{4+δ}. By increasing the concentration of Mn cations with a lower

valence state, oxygen vacancies form in the Ruddlesden-Popper structure, which improves the electrocatalytic activity for surface oxygen exchange and the diffusion of oxide ions. However, the precise quantification of Mn cations with mixed oxidation states is complex due to the complexity of Mn spectra. Therefore, the fitted peaks are mostly used to study the variation in cation valence state under different heat treatment conditions.

Conflicting interpretations of XPS spectra for O 1s in the literature make it difficult to investigate the oxygen species on the SPM surface [55,58,61]. According to an interpretation more consistent with our study, the O 1s spectra could be interpreted as two regions corresponding to the lattice oxygen at lower binding energies and surface components at higher binding energies [61–63]. The surface components comprise surface-adsorbed oxygen (O_2^- , O^-), surface carbonate, and hydroxyl [63]. It is necessary to highlight that the XPS-intensity peaks of the adsorbed species are directly related to the concentration of low coordination surface oxygen ions or oxygen defects [64]. Accordingly, the peak area at high binding energy could reflect the number of oxygen vacancies and interstitial oxygen close to the surface of the particles. It is also described that the formation of SrO on perovskite oxides results in a peak at around 530.6 eV associated with Sr–O and/or Sr–OH phases [56]. However, the complex character of formed secondary phases and physisorbed and chemisorbed oxygen components at high binding energy makes it difficult to specify their binding energy in O 1s spectra. For this reason, the peaks at high binding energy are called surface species or oxygen defects ($O_{S/D}$) in this work.

The O 1s spectra for both samples heat-treated in N_2 and humidified 5% H_2 in N_2 (Fig. 3d₁ and Fig. 3d₂, respectively) consist of a peak at low binding energy and a series of peaks at high binding energy. The lattice oxygen ($O_{Lat.}$) at the normal sites of the perovskite structure is located at 529.00 eV (Fig. 3d₁), while it is located at 528.80 eV (Fig. 3d₂) for the Ruddlesden-Popper structure [56,63]. Besides, the O 1s spectra for the Ruddlesden-Popper structure illustrate intensifying the peaks at high binding energies and dwindling the peak intensity corresponding to the lattice oxygen. Accordingly, the ratio of $O_{S/D}/O_{Lat.}$ increases from 1.05 in SPM perovskite to 1.75 in the reduced sample. The significant enhancement in the $O_{S/D}/O_{Lat.}$ ratio is mainly due to the characteristic feature of the Ruddlesden-Popper structure, which is associated with high concentrations and interstitial oxygen mobility, and is a significant factor in improving electrode performance for SOCs applications [65]. In addition, higher surface species and oxygen defects in the Ruddlesden-Popper structure resulting more active sites for electrocatalytic reactions in water electrolysis due to a higher tendency to adsorb oxygen species and hydroxyl group [19,66].

3.3. Microstructure investigation

Fig. 4 shows SEM images of an SPM electrode in a symmetric cell configuration, which is mechanically supported by the layered electrolyte. The ionic and electronic conductivity of the CGO layer above 600 °C can enhance the electrochemical performance of an electrode at elevated temperatures because the operation condition of the fuel electrode causes changes in the Ce ions oxidation state from Ce^{4+} to Ce^{3+} . However, reducing Ce ions increases the risk of an electronic leak above 700 °C. For this reason, a thin 10Sc1YSZ layer with a thickness of 7 μm makes it possible to mitigate this issue while maintaining high ionic conductivity through the layered electrolyte.

As shown, the prepared cell comprises dense layers in the electrolyte section, with excellent physicochemical binding between the CGO and 10Sc1YSZ layers, ensuring intimate attachment. Moreover, crack-free interfaces can enhance oxygen ions diffusion and consequently suppress double-layer resistance.

According to the microscopy images (Fig. 4.), a structurally integrated electrode can be created by screen printing the electrode material onto a dense electrolyte and sintered at a temperature of 1200 °C to create a structurally integrated electrode. The sintering temperature is

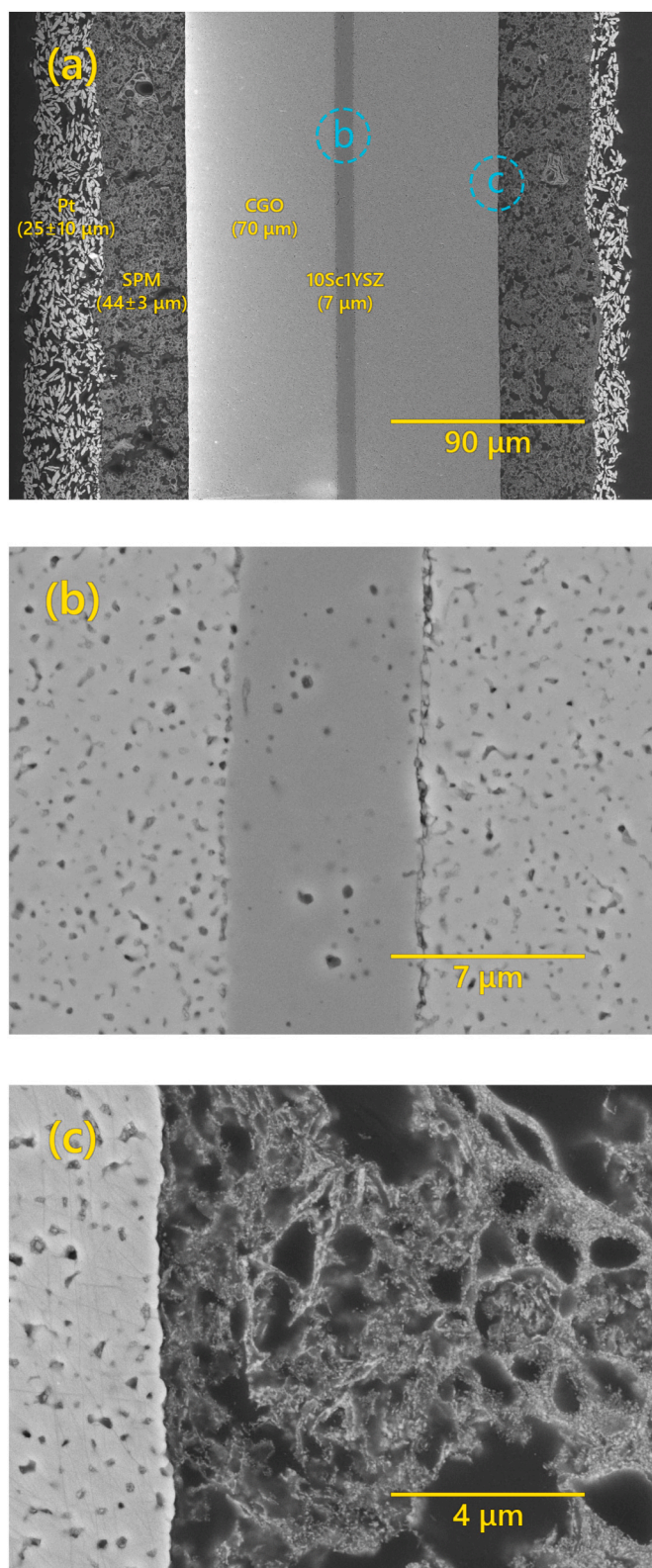


Fig. 4. SEM images of the SPM symmetric cell sintered at 1200 °C in the air. The location of images 4b and 4c with higher magnification is specified in Fig. 4a.

sufficiently high enough to form well-bonded electrode/electrolyte interfaces, resulting in mechanically robust cells for electrochemical performance. Despite this, the electrode microstructure comprises tiny particles with a mean size of 80 ± 25 nm. A combination of small

particles and open porosities ($1.2 \pm 0.9 \mu\text{m}$) in electrode microstructures improves electrode performance by providing numerous active sites and sufficient pathways for gas diffusion, respectively. Moreover, the modeling of cell performance versus electrode thickness revealed that the lowest polarization resistance for Ni-CGO fuel electrodes could be obtained when the electrode thickness is within the range of 10–50 μm [67]. Consequently, the prepared electrode with a thickness of $44 \pm 3 \mu\text{m}$ can enhance performance by offering a sufficient surface area for electrochemical reactions and minimizing the resistance associated with gas conversion.

The Pt layer with a large particle size works as a current collector to ensure an excellent electronic connection between the cell and the wires in the test setup, and it has a negligible effect on final electrochemical performance due to the distance from the electrolyte and thus the active part of the electrode.

3.4. Electrical conductivity

A four-point Van der Pauw method was used to study the electrical conductivity of the SPM electrode, which allows for the measurement of the average resistivity of any shape sample [68]. With the aim of determining the effect of phase transformation on the electrical conductivity of prepared samples, the measurements were carried out in the air and humidified 5% H_2 in N_2 gas. The obtained results in the air (Fig. 5a) show that the electrical conductivity of SPM perovskite steadily increases with temperature, reaching 41.4 S cm^{-1} at $800 \text{ }^\circ\text{C}$. Reflecting the semiconducting nature of electron conduction in SPM perovskite via localized electron holes called small polarons [69]. Once the electronic conductivity reached its maximum at $800 \text{ }^\circ\text{C}$ (marked by “M” in Fig. 5a), the sample was kept at the same temperature for 5 h to study any effect of dwell time, but a constant conductivity ($41.4 \pm 0.2 \text{ eV}$) over time. As the conductivity variation was negligible, the corresponding data for this period is shown with a green spot in Fig. 5a. The conductivity followed a similar trend during the cooling step as it did during the heating step. The slight hysteresis in the conductivity versus temperature profile at $650 \text{ }^\circ\text{C}$ might be caused by a slow change in the oxidation state of the cations not being able to reach full equilibrium during heating/cooling in this temperature range.

The electrical conductivity of SPM perovskite was further investigated in humidified 5% H_2 in N_2 gas after cooling the sample to room temperature (Fig. 5b). Upon heating the sample from room temperature to $310 \text{ }^\circ\text{C}$, the corresponding curve follows the same values as the one obtained from the measurement of conductivity in air. The obtained data in the air are replotted as a red dashed line for better comparison in Fig. 5b. The electrical conductivity at $310 \text{ }^\circ\text{C}$ is 5.8 S cm^{-1} . Further increasing the temperature leads to a steady decrease of electrical conductivity up to $460 \text{ }^\circ\text{C}$. The results show that conductivity is at its lowest value at this temperature. Reducing the oxidation state of the cations at elevated temperatures causes oxygen loss in the SPM structure.

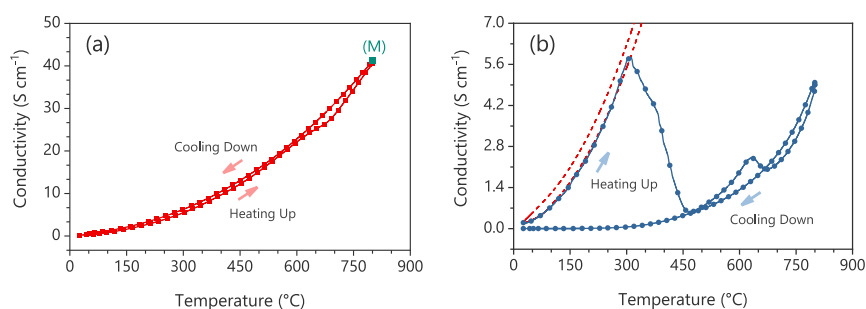


Fig. 5. Electrical conductivity of SPM perovskite from room temperature to $800 \text{ }^\circ\text{C}$ is measured in (a) air and (b) humidified 5% H_2 in N_2 atmospheres. The red dashed line in figure b represents the conductivity measurement in air shown in figure a. (For interpretation of the references to colour in this figure legend, the reader is referred to the Web version of this article.)

Consequently, the oxygen vacancies disturb transporting electron holes along B–O–B bonds and decrease the electrical conductivity [70, 71]. This result corroborates the XPS observation in Table 2, wherein the $\text{O}_{\text{S/D}}/\text{O}_{\text{Lat}}$ ratio increased due to reducing the average oxidation state of Mn cations for the heat-treated sample in the humidified 5% H_2 in N_2 atmosphere. Electron mobility is retarded by the reduction due to the increased concentration of positively charged oxide ion vacancies.

At higher temperatures, electrical conductivity increases as a function of temperature. However, further increasing the temperature above $630 \text{ }^\circ\text{C}$ (2.4 S cm^{-1}) causes an interruption in the conductivity improvement, as it decreases to 2.1 S cm^{-1} at $670 \text{ }^\circ\text{C}$. According to the XRD pattern in Fig. 1, the change in conductivity behavior coincides with perovskite to Ruddlesden-Popper transformation and formation of MnO and PrO_2 in the humidified 5% H_2 in N_2 atmosphere. Forming the Ruddlesden-Popper structure with a high oxygen vacancy concentration is expected to disturb the electronic conductivity. As the temperature rises, the electrical conductivity increases at a higher rate and reaches 5.0 S cm^{-1} at $800 \text{ }^\circ\text{C}$. The electrical conductivity of a sample at $800 \text{ }^\circ\text{C}$ does not change due to the 5 h dwell time, similar to the measurement in the air. The conductivity at this stage was at $5.0 \pm 0.1 \text{ S cm}^{-1}$. After that, no variation from semi-conductor behavior was observed during cooling. This steady conductivity decrease indicates no phase transformation in the Ruddlesden-Popper structure ($\text{SrPrMnO}_{4+\delta}$) while decreasing temperature from 800 to $25 \text{ }^\circ\text{C}$. It is important to note that the SPM perovskite has achieved the required conductivity level for SOEC electrodes ($>1 \text{ S cm}^{-1}$) both in air and humidified 5% H_2 in N_2 atmosphere [59].

3.5. Electrochemical performance

The electrochemical performance of the SPM electrode was studied with electrochemical impedance spectroscopy (EIS) in a wide range of pO_2 for the fuel electrode, e.g., $x\% \text{ H}_2\text{O}$ in H_2 ($x = 3, 10, 20$, and 50). Fig. 6 shows obtained impedance spectra for the SPM electrode at the different temperature ranges of 610 – $760 \text{ }^\circ\text{C}$. The frequency range in the EIS measurement was set from 10 mHz to 1 MHz to cover all electrochemical reactions in the prepared cell, and the inductance part at high frequency was removed from the equivalent circuit as this originates from the experimental setup rather than the cell. The impedance spectra in this study were fitted by two equivalent circuits of $R_\Omega(R_1Q_1)(R_2Q_2)$ or $R_\Omega(R_1Q_1)(R_2Q_2)(R_3Q_3)$, which were attributed to two or three different limiting processes in the cell. R_Ω is the ohmic resistance, mainly originating from the electrolyte, and the polarization resistance (R_p), is the sum of corresponding resistance for fitted arcs in the equivalent circuit, i.e., R_1+R_2 or $R_1+R_2+R_3$. The calculated summit frequency values for these reactions are in the high, medium, and low-frequency ranges. The variation of summit frequency and capacitance for fitted arcs versus temperature and gas composition are provided in the supplementary information (Fig. 2s).

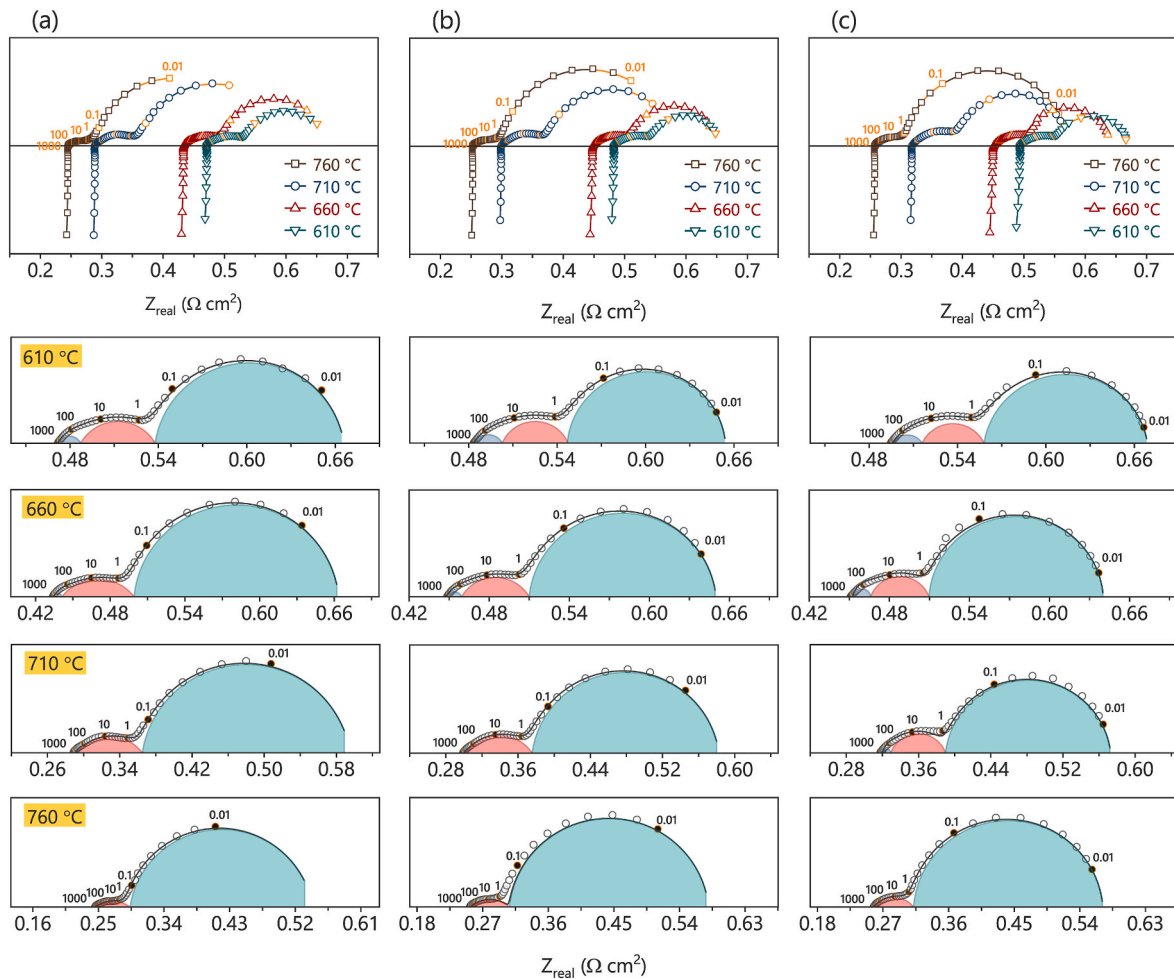


Fig. 6. Measured EIS spectra and breakdown of them by CNLS fitting to an equivalent circuit for the SPM electrode at different test temperatures in (a) 10% H₂O in H₂, (b) 20% H₂O in H₂, and (c) 50% H₂O in H₂. For each spectrum, the vertical axis starts at zero and is plotted using the same units and scale as the horizontal axis.

In order to quantify the electrochemical reactions of the Nyquist plots, CNLS (complex nonlinear least squares) fitting was performed using Zview software [72,73]. As the first step in the interpretation of sub-reactions in the EIS impedance, the resistance (R_i), constant phase element (Q_i), and frequency power (n_i) were extracted from the fitted equivalent circuit for each process. Then, for each arc represented by $R_i Q_i$, the R_i , Q_i , and n_i are used to calculate the summit frequency (F) and characteristic capacitance (C) at different testing conditions (Table 1s). Herein, the F and C are calculated using the following equations [74].

$$F = \frac{(R_i Q_i)^{-1/n_i}}{2\pi} \quad (3)$$

$$C = \frac{(R_i Q_i)^{1/n_i}}{R_i} \quad (4)$$

It is well-documented that electrode reactions may be complex and multistep processes [75]. The complexity of electrochemical reactions makes it challenging to interpret the individual reaction in the impedance spectrum. Moreover, the catalytic effect of steam concentration, the cell processing techniques, and phase transformation in electrode material could also affect the reaction kinetics [76,77]. Despite this, using reaction frequency and capacitance helps to classify the processes. Moreover, the variation of polarization resistance versus temperature and pO_2 in each reaction is a useful way to identify the nature of reactions. The possible reactions are connected with the charge transfer processes, gas diffusion, electrochemical surface reactions [78,79], and

electrochemical conversion processes in bulk parts of the cell, such as $Ce^{4+} + e^- \rightleftharpoons Ce^{3+}$ in the CGO electrolyte layers [80,81].

Fig. 7 gives an overview of ohmic resistance (R_Ω) and polarization resistance (R_p) broken down into resistances from fitted arcs (R_1 , R_2 , and R_3) at different test temperatures and gas compositions. The results show small R_p values for all investigated conditions. Note that the R_p values are the sum of R_p values for both electrodes in the symmetric cell and only half in a real cell with only one fuel electrode. In other words, the SPM perovskite electrode shows good electrocatalytic activity and electronic conductivity at different pO_2 of the investigated H₂O–H₂ gas mixtures. In contrast to other perovskite materials that deactivate with increasing pO_2 [11,82], high electrocatalytic activity over different gas compositions is the most notable characteristic of the SPM electrode.

Comparing the ohmic resistance in each temperature shows that the R_Ω decreases with decreasing steam concentration. This variation mainly originates from the CGO layer in the electrolyte, which significantly contributes to the ohmic resistance. At low steam concentrations, the number of Ce^{3+} increases due to the reduction of Ce^{4+} cations, and this causes a lower ohmic resistance in the ceria layers. The concentration of Ce^{4+} cations also decreases with increasing temperature in an atmosphere with low pO_2 [83]. Accordingly, the obtained results at 710 °C indicate a drop in ohmic resistance, but a thin 10Sc1YSZ layer in the layered electrolyte effectively prevents short circuits at elevated temperatures.

The deconvolution of the EIS spectra to sub-reactions (R_1 , R_2 , and R_3) shows that the low-frequency resistance (R_3) has the highest contribution to the polarization resistance (Fig. 7b). Moreover, increasing the

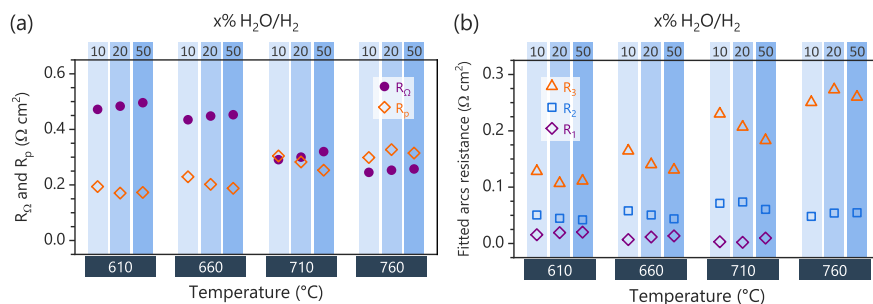


Fig. 7. The overview of (a) ohmic resistance (R_{Ω}), polarization resistance (R_p), and (b) resistance of fitted arcs (R_1 , R_2 , and R_3) for the electrochemical performance of the SPM electrode in different gas compositions and temperatures.

resistance for this contribution increases with temperature. At the same time, the high-frequency reaction (R_1) decreased with temperature and reached zero at 760 °C. The resistance of the reaction at the medium frequency (R_2) remains at the same order of magnitude over the investigated range of conditions. Further details about the sub-reactions and fitted arcs are discussed in the following.

The HF reaction (R_1Q_1) is fitted with an arc having a summit frequency within a wide range of frequencies in the EIS spectra. Besides, the calculated capacitance for this reaction is about 10^{-3} – 10^{-2} F cm^{-2} and does not change substantially with the measured temperature (Table 1s). According to the fitted values, the summit frequency for this reaction gradually increases with the test temperature from 44 Hz to 408 Hz. It is also reported that the high-frequency reaction in the $\text{La}_{0.5}\text{Sr}_{1.5}\text{MnO}_{4\pm\delta}$ Ruddlesden-Popper underwent a similar behavior when tested in H_2 with 3% H_2O [35].

The activation energy of the polarization resistance and fitted arcs for the electrochemical performance of the SPM electrode in all investigated gas compositions are provided in Fig. 3s. The calculated activation energy for the first reaction (R_1Q_1) indicates a high thermally activated process (0.66–1.56 eV). This wide activation range is primarily due to the large fitting uncertainty since the arc size is significantly reduced by increased temperatures. It was attempted to fit the impedance spectra with $R_{\Omega}(R_1Q_1)(R_2Q_2)$ reaction, but it caused much worse fitting results.

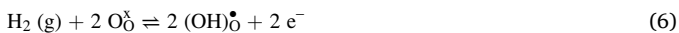
The fitting parameters for the R_1Q_1 at high-frequency regions represent the characteristic features of the charge transfer process with high activation energy [35,84]. However, the calculated capacitance (10^{-2} – 10^{-3} F cm^{-2}) is higher than the magnitude of the interfacial capacitance. This points towards a redox process in the electrode material, i.e., changes in the oxidation states of Mn- and Pr-ions. Even though numerous studies have been conducted on the charge transfer process, it remains one of the least understood aspects of electrochemistry for MIEC materials [85].

The overall water electrolysis reaction on the fuel side of the SOEC cell can be described as the following reaction [86].

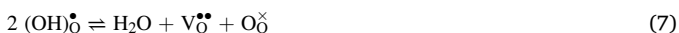


According to the Kröger-Vink notation, the $\text{V}_{\text{O}}^{\bullet\bullet}$ and $\text{O}_{\text{O}}^{\times}$ denote an oxygen vacancy and regular lattice oxygen in SPM oxide, respectively.

The charge transfer reaction has primarily been studied for the state-of-the-art Ni-YSZ electrode, where the oxidation reaction is assumed to occur near the 3PB. At the same time, several different mechanisms have been proposed to explain the actual pathway or the nature of the elementary steps. The first reaction is dissociative adsorption/associative desorption that proceeds on the SPM electrode surface [86,87].



The next reaction on the surface is



and the oxide vacancy is after that transferred to/from the bulk SPM oxide and to/from the electrolyte. Thus, R_1 is assumed to originate from O^{2-} conduction resistance in the SPM layer, and the capacitance of Q_1 originates from the change in SPM composition with the variation of the overpotential during the EIS measurement.

Our investigation of the dependence of the charge transfer reaction on the gas composition reveals an additional effect as a function of $p\text{O}_2$. A possible explanation for such behavior in the HF reaction is likely related to the variation of oxide vacancy concentration. The improvement of the HF process was also reported for the CGO-infiltrated fuel electrode before, in which the oxide charge transfer resistance decreased by improving the conduction of oxide ions through the mesh-like CGO layer [88].

As discussed earlier, after forming the SPM perovskite at 1000 °C in an N_2 atmosphere with $p\text{O}_2 = 6.37 \times 10^{-7}$ atm., its crystal structure remains perovskite when it is heat-treated for a second time in humidified H_2 atmosphere at 600 °C (Fig. 1). Nevertheless, the perovskite structure started transforming to Ruddlesden-Popper when increasing the temperature above 600 °C. The Rietveld refinement demonstrated 63 wt% of SPM perovskite transforms to Ruddlesden-Popper above 660 °C. Accordingly, it can be concluded that there is a mixture of two structures while measuring the impedance spectra in the temperature range of 610–760 °C. The ratio of Ruddlesden-Popper to perovskite structure (RP:P) depends on test temperature and $p\text{O}_2$, and the oxygen content (oxide vacancy concentration) in both phases will also depend on $p\text{O}_2$.

At elevated temperatures where the RP:P ratio increases, the oxide ion's conductivity might increase due to the low activation energy required for interstitial oxygen conductivity in the Ruddlesden-Popper structure and the high concentration of oxygen vacancies in reduced perovskite structure [89]. As a result, the fitted arcs for all investigated conditions at 710 °C show negligible resistance for this reaction, and the corresponding resistance was not measurable at 760 °C.

In summary, the charge transfer process for the SPM fuel electrode is considered as the $\text{H}_2(\text{g})$ reaction with the SPM electrode surface plus the oxide ion transport through the SPM plus the interfacial oxide ion charge transfer at the electrode/electrolyte interface. Presumably, this HF part of the impedance is dominated by the O^{2-} transport resistance through the SPM electrode layer in parallel with the chemical capacitance of the SPM electrode.

The second process (R_2Q_2) in the electrochemistry of the SPM electrode is fitted with an arc at medium-frequency (MF) in the 4–13 Hz range. The Arrhenius plot in all investigated gas compositions indicates that the R_2Q_2 is a slightly thermally deactivated process with an apparent “activation energy” range from -0.09 to -0.06 eV (Fig. 3s). Furthermore, the equivalent capacitance for this process is in the range of 10–40 mF cm^{-2} for all studied conditions, which cannot be attributed to interfacial capacitance. Although the resulting capacitance is compatible with the dissociative adsorption of hydrogen on the electrode surface, it is known that DAH is a thermally activated reaction

with an activation energy of about 0.47 eV [90]. From the literature, the MF resistance could be caused by mass transfer (including gas diffusion and surface diffusion) or gas conversion [35,91].

The gas diffusion process is characterized by a slightly thermally-activated resistance with activation energy close to zero [77]. The frequency range for this process is reported at around 10–100 Hz [17] and is influenced strongly by steam concentration, particularly in the low steam and low hydrogen partial pressure ranges [72]. Mohammad Hussain et al. [18], in their study on gas diffusion impedance of Nb-doped SrTiO₃, found that increasing the H₂O concentration from 1% to 3% leads to decreasing the polarization resistance by three orders of magnitude. Similar behavior was also reported for the Ni-ScYSZ electrode with varying steam concentrations from 3% to 80% [72].

In light of the characteristics of the gas diffusion process, there is a significant difference between the gas diffusion process and the MF process in this study. Since MF resistance shows its independence from steam concentration (Fig. 5s), the Arrhenius plot indicates a slightly thermally deactivated process.

The MF reaction is likely related to the gas conversion process with relatively high capacitance and a slight negative “activation energy”. The cause of this resistance is an accumulation of reaction product and depletion of reactant outside the active electrode surface in case the gas transport (gas flow, diffusion, convection) is too slow to keep the initial reactant partial pressure values. In other words, the Nernst potential of the electrode will not be kept constant [92]. According to previous reports, the capacitance of the gas conversion reaction ranged from 0.01 to 1 F cm⁻² [93], which agrees with the value obtained in this work. Nevertheless, it depends on several experimental conditions, including gas flow rate, cell setup geometry, partial gas, and overall gas pressure.

The third process (R₃Q₃) with a large capacitance (0.5–2.7 F cm⁻²) was fitted by an arc at a low frequency (LF) range of 0.01–0.07 Hz. The Arrhenius plot of this reaction reveals a thermally deactivated reaction with an apparent “activation energy” of –0.29 eV in 10% H₂O in H₂ gas (Fig. 3s). The LF resistance probably originates from the two thick CGO electrolyte layers (70 μm each) in the symmetric cell. The chemical capacitance caused by the reduction/oxidation of Ce ions (Eq. (9)) is responsible for the huge capacitance in Q₃ under reducing conditions.



In other words, the chemical capacitance originates from changing the chemical composition of cell components under fuel electrode conditions [12,94] and is generally observed in a mixed ionic and electronic conductor (MIEC). Operating the current cell in a reducing atmosphere causes a deviation from the stoichiometry of the oxygen content in the CGO layer, which can be significant and detectable as a low-frequency response in impedance spectra [95].

The non-stoichiometry oxygen content under reducing conditions has two significant effects on impedance spectra in contrast to the idealized response of a purely ionic layer. First, electronic conductivity acts as an additional resistance in parallel with ionic impedances. Second, the corresponding resistance shifts to a much lower frequency [95]. This is why the corresponding arc at low frequency has not been completed when chemical capacitance increases with testing the electrode at lower steam concentrations. It is necessary to highlight that reliable values of electrode capacitance cannot be obtained under such conditions unless the electrode capacitance is substantial.

A chemical capacitance was also reported previously for a symmetric Sr₂FeMn_{0.5}Mo_{0.5}O₆ (SFMM) perovskite electrode [12]. Where replacing the 10Sc1CeSZ electrolyte with a layered electrolyte (containing a thin yttria-stabilized zirconia (YSZ) layer supported by a thick CGO layer), a resistance at low frequencies was observed along with high capacitance. In this case, the polarization resistance due to chemical capacitance is directly proportional to the layer thickness. Jamnik et al. [96] and Lai et al. [97] have provided further details about the corresponding circuit and electrochemical mechanisms behind this phenomenon.

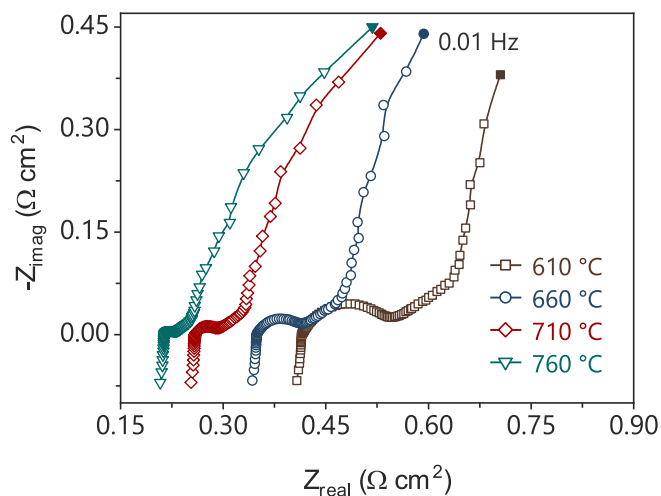


Fig. 8. The impedance spectra of the SPM electrode in 3% H₂O in H₂ at 610, 660, 710, and 760 °C.

However, the high resistance (and the large capacitance) of the thick CGO layers is not to be expected in a technological cell, where the structural component typically would be a zirconia-based structure (fuel electrode-supported cell with a thin electrolyte) or metallic-based fuel electrode support. Thus, this contribution to the R_p can be disregarded in such technological cells.

Fig. 8 shows the impedance spectra for the cell tested at different temperatures in 3% H₂O in H₂. The pO₂ for this measurement varies from 2.77 × 10⁻²⁷ atm at 610 °C to 4.95 × 10⁻²³ atm at 760 °C. It is evident that the SPM electrode exhibits a considerable polarization resistance in highly reducing atmospheres, i.e., 3% H₂O in H₂. As the frequency decreases below 0.1 Hz, both the real and imaginary components of the impedance increase, indicating that the SPM electrode functions as a blocking layer in 3% H₂O in H₂ compared to its performance under higher steam concentrations. The underlying cause of this phenomenon remains unknown, but the EIS of the SPM electrodes in this reducing gas mixture suggests that the outer surface of the SPM electrode is almost blocking the current. A possible explanation might be that the pores in the SPM electrode were blocked partially by chemical expansion on the reduction of the SPM material. It is assumed that blocking occurs within the outer part of the electrode because all parts of the EIS of the high-performance and less reduced electrodes can be seen at frequencies above 1 Hz, below which the R₃Q₃ arc becomes overlaid by steeply increasing imaginary impedance values. At higher frequencies, the huge capacitance of the CGO layers was enough to supply the necessary oxygen change for the variation in the electrode potential required for the AC current through the SPM electrodes.

It is important to note that for a practical cell operated in SOFC mode, the SPM fuel electrode will normally have a significantly more oxidizing potential than 3% H₂O in H₂ due to the anodic polarization. In the case of SOEC mode, it will be essential to ensure that the negative potential of the cathodic polarized SPM electrode never becomes as negative as the potential of 3% H₂O in H₂. As a SOEC is supposed to be operated with about 20% H₂O at the outlet, it should be possible to avoid excessive reduction of an SPM electrode with very low polarization resistance.

4. Conclusions

This work considers the development of a nickel-free fuel electrode for solid oxide cells, specifically the Sr_{0.5}Pr_{0.5}MnO₃ (SPM) perovskite. The electrochemical performance of the SPM electrode was measured in a wide range of steam concentrations from 3% to 50% H₂O in H₂ using a symmetric cell with a layered electrolyte containing thick CGO layers in

its structure. The impedance spectra of the cell at open circuit voltage in the gas composition of 50% H₂O in H₂ demonstrate a minimal polarization resistance of 0.173 Ω cm² at 610 °C, increasing to 0.315 Ω cm² at 760 °C. The complex nonlinear least squares fitting of the Nyquist plots demonstrated that increased polarization resistance by temperature is primarily due to increasing the low-frequency resistance at elevated temperatures. The Low-frequency resistance with high capacitance and apparent negative activation energy most probably originates from (i) the changing of the stoichiometry of oxygen in the CGO layer, which increases the Ce³⁺ concentration, and (ii) forming an AC current blocking layer in the SPM electrode using 3% H₂O in H₂. The deviation from the stoichiometry content of the oxygen in the CGO layer is responsible for high chemical capacitance, and increased low-frequency resistance can be attributed to unknown phase evolution and structural expansion in the SPM electrode under studied gas mixtures.

However, replacing the thick CGO layers used in this cell with a standard thin CGO barrier layer in the technological cell can exclude high chemical capacitance from electrode performance, and operating the cell at 610 °C suppresses the phase transformation expansion and maintains phase stability. The high electrocatalytic activity of the SPM perovskite in 50% H₂O in H₂ makes it a potential candidate for lowering the operating temperature of solid oxide cells to 610 °C in both SOFC and SOEC applications.

The investigation of phase evolution using Rietveld refinement showed the formation of SPM perovskite with heat treatment of the powder at 1000 °C in N₂ gas with pO₂ of 6.37 × 10⁻⁷ atm. It was also determined that the heat treatment of the SPM perovskite above 600 °C in humidified 5% H₂ in N₂ atmosphere leads the perovskite to Ruddlesden-Popper transformation with I4/mmm (139) space group. This transformation resulted in an increase in the c parameter in the crystal structure while the other lattice parameters remained in the same order of magnitude. Using the number of ions calculated through site occupancy in Rietveld refinement and the crystal volume for both structures, an expansion of 0.28% was calculated for perovskite to Ruddlesden-Popper phase transformation.

The XPS spectra revealed that the perovskite to Ruddlesden-Popper transformation increases the concentration of oxygen defects. Accordingly, the quantitative analysis of O 1s spectra showed that this phase transformation increased the O_{S/D}/O_{Lat} ratio from 1.05 to 1.75. Increasing surface species or oxygen defects in the O 1s spectra are mainly due to the characteristic feature of the Ruddlesden-Popper structure with a high concentration of interstitial oxide ions, which can provide high ionic conductivity in fuel electrode working conditions. Additionally, the presence of multivalent Mn and Pr cations enhances the electronic conductivity of the developed electrode by increasing the number of polarons.

The microscopy images demonstrated crack-free interfaces for the prepared three-layered CGO|10Sc1YSZ|CGO substrate. Besides, small particles (with a mean particle size of 80 ± 25 nm) and the porous structure (with a pore size of 1.2 ± 0.9 μm) in the fuel electrode can provide high surface area and proper gas diffusion channels.

Finally, our proposed approach offers two key strategies to address the concern of scarcity of Sr and Pr cations used in the developed SPM electrode. By selective substitution of Pr with other lanthanide elements, we can reduce the demand for Pr while maintaining desired properties. Additionally, employing a thin electrode layer enables more efficient utilization of Sr and Pr, reducing their overall consumption. These combined approaches offer a sustainable and commercially viable solution, contributing to advancing environmentally friendly energy technologies.

CRedit authorship contribution statement

Yousef Alizad Farzin: Writing – original draft, Conceptualization, Methodology, Investigation, Formal analysis, Visualization. **Mogens Bjerg Mogensen:** Writing – review & editing, Supervision. **Stéven**

Pirou: Writing – review & editing, Investigation. **Henrik Lund Frandsen:** Writing – review & editing, Supervision, Conceptualization, Resources, Project administration, Funding acquisition.

Declaration of competing interest

The authors declare that they have no known competing financial interests or personal relationships that could have appeared to influence the work reported in this paper.

Data availability

The authors are unable or have chosen not to specify which data has been used.

Acknowledgment

The authors would like to thank the financial support of this study, which was funded by the Innovation Fund Denmark (IFD) under File No. 9067-00036B REFORGE.

Appendix A. Supplementary data

Supplementary data to this article can be found online at <https://doi.org/10.1016/j.jpowsour.2023.233450>.

References

- [1] V. Vibhu, I.C. Vinke, R.A. Eichel, L.G.J. de Haart, Cobalt substituted Pr₂Ni_{1-x}CoxO_{4+δ} (x = 0, 0.1, 0.2) oxygen electrodes: impact on electrochemical performance and durability of solid oxide electrolysis cells, *J. Power Sources* 482 (2021), <https://doi.org/10.1016/j.jpowsour.2020.228909>.
- [2] N. Mahato, A. Banerjee, A. Gupta, S. Omar, K. Balani, Progress in material selection for solid oxide fuel cell technology: a review, *Prog. Mater. Sci.* 72 (2015) 141–337, <https://doi.org/10.1016/j.pmatsci.2015.01.001>.
- [3] J. Zhang, C. Lenser, N.H. Menzler, O. Guillon, Comparison of solid oxide fuel cell (SOFC) electrolyte materials for operation at 500 °C, *Solid State Ionics* 344 (2020), 115138, <https://doi.org/10.1016/J.SSI.2019.115138>.
- [4] C. Lenser, J. Zhang, N. Russner, A. Weber, O. Guillon, N.H. Menzler, Electro-chemo-mechanical analysis of a solid oxide cell based on doped ceria, *J. Power Sources* 541 (2022), 231505, <https://doi.org/10.1016/J.JPOWSOUR.2022.231505>.
- [5] W.C. Chueh, Y. Hao, W. Jung, S.M. Haile, High electrochemical activity of the oxide phase in model ceria–Pt and ceria–Ni composite anodes, *Nat. Mater.* 112 (11) (2011) 155–161, <https://doi.org/10.1038/nmat3184>, 2011.
- [6] A. Hauch, K. Brodersen, M. Chen, M.B. Mogensen, Ni/YSZ electrodes structures optimized for increased electrolysis performance and durability, *Solid State Ionics* 293 (2016) 27–36, <https://doi.org/10.1016/j.ssi.2016.06.003>.
- [7] M.B. Mogensen, M. Chen, H.L. Frandsen, C. Graves, A. Hauch, P.V. Hendriksen, T. Jacobsen, S.H. Jensen, T.L. Skaftø, X. Sun, Ni migration in solid oxide cell electrodes: review and revised hypothesis, *Fuel Cell* 21 (2021) 415–429, <https://doi.org/10.1002/FUCE.202100072>.
- [8] N.H. Menzler, D. Sebold, Y.J. Sohn, S. Zischke, Post-test characterization of a solid oxide fuel cell after more than 10 years of stack testing, *J. Power Sources* 478 (2020), 228770, <https://doi.org/10.1016/J.JPOWSOUR.2020.228770>.
- [9] L. Wang, Y. Yu, K.J. Gaskell, E.J. Crumlin, Z. Liu, B.W. Eichhorn, G.S. Jackson, In operando x-ray photoelectron spectroscopy studies of H₂ oxidation and H₂O electrolysis on gadolinia-doped ceria electrodes, *J. Phys. Energy* 3 (2021), <https://doi.org/10.1088/2515-7655/ABC354>.
- [10] V. Vibhu, I.C. Vinke, F. Zavelis, S.G. Neophytides, D.K. Niakolas, R.A. Eichel, L.G. J. de Haart, Performance and degradation of electrolyte-supported single cell composed of Mo–Au–Ni/GDC fuel electrode and LSCF oxygen electrode during high temperature steam electrolysis, *Energies* 15 (2022), <https://doi.org/10.3390/EN15082726>.
- [11] Y.A. Farzin, A. Babaei, T.L. Skaftø, E. Stamate, A. Ataie, S.H. Jensen, Low-temperature preparation and investigation of electrochemical properties of SFM/CGO composite electrode, *Solid State Ionics* 356 (2020), 115435, <https://doi.org/10.1016/j.ssi.2020.115435>.
- [12] Y. Alizad Farzin, A. Babaei, T. Løye Skaftø, E. Stamate, A. Ataie, S.H. Jensen, Development of an SFMM/CGO composite electrode with stable electrochemical performance at different oxygen partial pressures, *Int. J. Hydrogen Energy* 47 (2022) 7915–7931, <https://doi.org/10.1016/J.IJHYDENE.2021.12.104>.
- [13] T. Yao, N. Hou, J. Gan, J. Wang, X. Zhi, L. Fan, T. Gan, Y. Zhao, Y. Li, Enhanced activity and stability of Sr₂FeMo_{0.65}Ni_{0.35}O_{6-Δ} anode for solid oxide fuel cells with Na doping, *J. Power Sources* 425 (2019) 103–109, <https://doi.org/10.1016/j.jpowsour.2019.04.004>.

- [14] Y.A. Farzin, A. Weber, M. Harenbrock, D. Nardini, Effective suppression of LSCF air electrode degradation by air cleaning, *ECS Trans.* 111 (2023) 1987, <https://doi.org/10.1149/11106.1987ECST>.
- [15] F.E. Winterhalder, Y. Alizad Farzin, O. Guillon, A. Weber, N.H. Menzler, Perovskite-based materials as alternative fuel electrodes for solid oxide electrolysis cells (SOECs), *ECS Trans.* 111 (2023) 1115–1123, <https://doi.org/10.1149/11106.1115ecst>.
- [16] S. Tao, J.T.S. Irvine, A redox-stable efficient anode for solid-oxide fuel cells, *Nat. Mater.* 2 (2003) 320–323, <https://doi.org/10.1038/nmat871>.
- [17] X.M. Ge, S.H. Chan, Lanthanum strontium vanadate as potential anodes for solid oxide fuel cells, *J. Electrochem. Soc.* 156 (2009) B386, <https://doi.org/10.1149/1.3058585/XML>.
- [18] A. Mohammed Hussain, J.V.T. Høgh, T. Jacobsen, N. Bonanos, Nickel-ceria infiltrated Nb-doped SrTiO₃ for low temperature SOFC anodes and analysis on gas diffusion impedance, *Int. J. Hydrogen Energy* 37 (2012) 4309–4318, <https://doi.org/10.1016/j.ijhydene.2011.11.087>.
- [19] S. Chen, Y. Hao, R. Chen, Z. Su, T. Chen, Hollow multishelled spherical PrMnO₃ perovskite catalyst for efficient catalytic oxidation of CO and toluene, *J. Alloys Compd.* 861 (2021), <https://doi.org/10.1016/j.jallcom.2020.158584>.
- [20] S. Chen, H. Li, Y. Hao, R. Chen, T. Chen, Porous Mn-based oxides for complete ethanol and toluene catalytic oxidation: the relationship between structure and performance, *Catal. Sci. Technol.* 10 (2020) 1941–1951, <https://doi.org/10.1039/C9CY02522G>.
- [21] A. Kaddouri, P. Gelin, N. Dupont, Methane catalytic combustion over La–Ce–Mn–O perovskite prepared using dielectric heating, *Catal. Commun.* 10 (2009) 1085–1089, <https://doi.org/10.1016/J.CATCOM.2008.12.063>.
- [22] G. Liu, J. Li, K. Yang, W. Tang, H. Liu, J. Yang, R. Yue, Y. Chen, Effects of cerium incorporation on the catalytic oxidation of benzene over flame-made perovskite La_{1-x}Ce_xMnO₃ catalysts, *Particuology* 19 (2015) 60–68, <https://doi.org/10.1016/J.PARTIC.2014.07.001>.
- [23] X. Huang, M. Li, Hard-templating synthesis of mesoporous La_{1-x}Sr_xMnO_{3+δ} Perovskite and catalysis activity in CO oxidation, *Adv. Mater. Res.* 306–307 (2011) 1342–1349, <https://doi.org/10.4028/WWW.SCIENTIFIC.NET/AMR.306-307.1342>.
- [24] H. Lv, Y. Zhou, X. Zhang, Y. Song, Q. Liu, G. Wang, X. Bao, Infiltration of Ce_{0.8}Gd_{0.2}O_{1.9} nanoparticles on Sr₂Fe_{1.5}Mo_{0.5}O_{6-δ} cathode for CO₂ electroreduction in solid oxide electrolysis cell, *J. Energy Chem.* 35 (2019) 71–78, <https://doi.org/10.1016/j.jechem.2018.11.002>.
- [25] S.P. Jiang, A review of wet impregnation—an alternative method for the fabrication of high performance and nano-structured electrodes of solid oxide fuel cells, *Mater. Sci. Eng.* 418 (2006) 199–210, <https://doi.org/10.1016/J.MSEA.2005.11.052>.
- [26] Z. Sun, W. Fan, Y. Bai, K. Wu, Y. Cheng, Tailoring electrochemical performance of perovskite anodes through in situ exsolution of nanocatalysts, *ACS Appl. Mater. Interfaces* 13 (2021) 29755–29763, <https://doi.org/10.1021/ACSAMI.1C08396>.
- [27] P.B. Managutti, S. Tymen, X. Liu, O. Hernandez, C. Prestipino, A.L.G. La Salle, S. Paul, L. Jalowiecki-Duhamel, V. Dorcet, A. Billard, P. Briois, M. Bahout, Exsolution of Ni nanoparticles from A-site-deficient layered double perovskites for dry reforming of methane and as an anode material for a solid oxide fuel cell, *ACS Appl. Mater. Interfaces* 13 (2021) 35719–35728, <https://doi.org/10.1021/ACSAMI.1C08158>.
- [28] W. Fan, Z. Sun, Y. Bai, K. Wu, J. Zhou, Y. Cheng, In situ growth of nanoparticles in A-site deficient ferrite perovskite as an advanced electrode for symmetrical solid oxide fuel cells, *J. Power Sources* 456 (2020), 228000, <https://doi.org/10.1016/J.JPOWSOUR.2020.228000>.
- [29] S. Kim, G. Kim, A. Manthiram, A review on infiltration techniques for energy conversion and storage devices: from fundamentals to applications, *Sustain. Energy Fuels* 5 (2021) 5024–5037, <https://doi.org/10.1039/D1SE00878A>.
- [30] S. Sengodan, Y.W. Ju, O. Kwon, A. Jun, H.Y. Jeong, T. Ishihara, J. Shin, G. Kim, Self-decorated MnO nanoparticles on double perovskite solid oxide fuel cell anode by in situ exsolution, *ACS Sustain. Chem. Eng.* 5 (2017) 9207–9213, <https://doi.org/10.1021/acsuschemeng.7b02156>.
- [31] D. Neagu, G. Tsekouras, D.N. Miller, H. Ménard, J.T.S. Irvine, In situ growth of nanoparticles through control of non-stoichiometry, *Nat. Chem.* 2013 511 (5) (2013) 916–923, <https://doi.org/10.1038/nchem.1773>.
- [32] K. Svoboda, A. Siewiorek, D. Baxter, J. Rogut, M. Puncóchár, Thermodynamic possibilities and constraints of pure hydrogen production by a chromium, nickel, and manganese-based chemical looping process at lower temperatures, *Chem. Pap.* 612 (61) (2007) 110–120, <https://doi.org/10.2478/S11696-007-0007-6>, 2007.
- [33] D. Lee, D. Kim, S.J. Son, Y. il Kwon, Y. Lee, J.H. Ahn, J.H. Joo, Simultaneous A- and B-site substituted double perovskite (AA'B₂O_{5+δ}) as a new high-performance and redox-stable anode material for solid oxide fuel cells, *J. Power Sources* 434 (2019), 226743, <https://doi.org/10.1016/j.jpowsour.2019.226743>.
- [34] A.C. Tomkiewicz, M.A. Tamimi, A. Huq, S. McIntosh, Structural analysis of PrBaMn₂O_{5+δ} under SOFC anode conditions by in-situ neutron powder diffraction, *J. Power Sources* 330 (2016) 240–245, <https://doi.org/10.1016/j.jpowsour.2016.09.013>.
- [35] M.V. Sandoval, C. Cardenas, E. Capoen, P. Roussel, C. Pirovano, G.H. Gauthier, Performance of La_{0.5}Sr_{1.5}MnO_{4±δ} Ruddlesden-Popper manganite as electrode material for symmetrical solid oxide fuel cells. Part B. the hydrogen oxidation reaction, *Electrochim. Acta* 353 (2020), <https://doi.org/10.1016/j.electacta.2020.136494>.
- [36] L. Duranti, I. Natali Sora, F. Zurlo, I. Luisetto, S. Licoccia, E. Di Bartolomeo, The role of manganese substitution on the redox behavior of La_{0.6}Sr_{0.4}Fe_{0.8}Mn_{0.2}O_{3-δ}, *J. Eur. Ceram. Soc.* 40 (2020) 4076–4083, <https://doi.org/10.1016/j.jeurceramsoc.2020.04.017>.
- [37] Y.F. Sun, Y.Q. Zhang, B. Hua, Y. Behnamian, J. Li, S.H. Cui, J.H. Li, J.L. Luo, Molybdenum doped Pr_{0.5}Ba_{0.5}MnO_{3-δ} (Mo-PBMO) double perovskite as a potential solid oxide fuel cell anode material, *J. Power Sources* 301 (2016) 237–241, <https://doi.org/10.1016/j.jpowsour.2015.09.127>.
- [38] Y. Alizad Farzin, O. Mirzaee, A. Ghasemi, Synthesis behavior and magnetic properties of Mg-Ni co-doped Y-type hexaferrite prepared by sol-gel auto-combustion method, *Mater. Chem. Phys.* 178 (2016) 149–159, <https://doi.org/10.1016/j.matchemphys.2016.04.082>.
- [39] E. Hosseinkhan Nejad, Y.A. Farzin, M.A. Heydari, Enhancement of soft magnetic properties of La–Zn co-doped nanocrystalline Ni₂Y hexaferrite, *J. Magn. Magn. Mater.* 423 (2017) 226–231, <https://doi.org/10.1016/j.jmmm.2016.09.097>.
- [40] Y.A. Farzin, A. Babaei, A. Ataie, Low-temperature synthesis of Sr₂FeMoO₆ double perovskite; structure, morphology, and magnetic properties, *Ceram. Int.* 46 (2020) 16867–16878, <https://doi.org/10.1016/j.ceramint.2020.03.264>.
- [41] Y. Alizad Farzin, O. Mirzaee, A. Ghasemi, Influence of Mg and Ni substitution on structural, microstructural and magnetic properties of Sr₂Co_{2-x}Mg_x/2Ni_x/2Fe_{1-2x}2O₂₂ (Co₂Y) hexaferrite, *J. Magn. Magn. Mater.* 371 (2014) 14–19, <https://doi.org/10.1016/j.jmmm.2014.07.007>.
- [42] H. Kim, C. Lim, O. Kwon, J. Oh, M.T. Curnan, H.Y. Jeong, S. Choi, J.W. Han, G. Kim, Unveiling the key factor for the phase reconstruction and exsolved metallic particle distribution in perovskites, *Nat. Commun.* 121 (12) (2021) 1–11, <https://doi.org/10.1038/s41467-021-26739-1>, 2021.
- [43] Y.S. Chung, T. Kim, T.H. Shin, H. Yoon, S. Park, N.M. Sammes, W.B. Kim, J. S. Chung, In situ preparation of a La_{1.2}Sr_{0.8}Mn_{0.4}Fe_{0.6}O₄ Ruddlesden-Popper phase with exsolved Fe nanoparticles as an anode for SOFCs, *J. Mater. Chem. A* 5 (2017) 6437–6446, <https://doi.org/10.1039/C6TA09692A>.
- [44] Z. Zhong, Z. Li, J. Li, X. Guo, Q. Hu, Y. Feng, H. Sun, A facile method to synthesize BaZr_{0.1}Ce_{0.7}Y_{0.1}Yb_{0.1}O_{3-δ} (BZCY₁Yb) nanopowders for the application on highly conductive proton-conducting electrolytes, *Int. J. Hydrogen Energy* 47 (2022) 40054–40066, <https://doi.org/10.1016/J.IJHYDENE.2022.09.149>.
- [45] T. Liu, Y. Zhao, X. Zhang, H. Zhang, G. Jiang, W. Zhao, J. Guo, F. Chen, M. Yan, Y. Zhang, Y. Wang, Robust redox-reversible perovskite type steam electrolyser electrode decorated with in situ exsolved metallic nanoparticles, *J. Mater. Chem. A* 8 (2020) 582–591, <https://doi.org/10.1039/C9TA06309A>.
- [46] X. Zhang, Y. Tong, T. Liu, D. Zhang, N. Yu, J. Zhou, Y. Li, X.-K. Gu, Y. Wang, C. Tong Liu, K. Gu, Robust Ruddlesden-Popper phase Sr₃Fe_{1.3}Mo_{0.5}Ni_{0.2}O_{7-δ} decorated with in-situ exsolved Ni nanoparticles as an efficient anode for hydrocarbon fueled solid oxide fuel cells, *SusMat* 2 (2022) 487–501, <https://doi.org/10.1002/SUS2.58>.
- [47] D. Zhang, Y. Wang, Y. Peng, Y. Luo, T. Liu, W. He, F. Chen, M. Ding, Novel high-entropy perovskite-type symmetrical electrode for efficient and durable carbon dioxide reduction reaction, *Adv. Powder Mater.* 2 (2023), 100129, <https://doi.org/10.1016/J.APMATE.2023.100129>.
- [48] C. Chatzichristodoulou, P. Norby, P.V. Hendriksen, M.B. Mogensen, Size of oxide vacancies in fluorite and perovskite structured oxides, *J. Electroceram.* 34 (2015) 100–107, <https://doi.org/10.1007/S10832-014-9916-2/FIGURES/6>.
- [49] T. Nakamura, R. Oike, Y. Ling, Y. Tamenori, K. Amezawa, The determining factor for interstitial oxygen formation in Ruddlesden-Popper type La₂NiO₄-based oxides, *Phys. Chem. Chem. Phys.* 18 (2016) 1564–1569, <https://doi.org/10.1039/C5CP05993C>.
- [50] H. Ullmann, N. Trofimenko, F. Tietz, D. Stöver, A. Ahmad-Khanlou, Correlation between thermal expansion and oxide ion transport in mixed conducting perovskite-type oxides for SOFC cathodes, *Solid State Ionics* 138 (2000) 79–90, [https://doi.org/10.1016/S0167-2738\(00\)00770-0](https://doi.org/10.1016/S0167-2738(00)00770-0).
- [51] S.P.S. Shaikh, A. Muchtar, M.R. Somalu, A review on the selection of anode materials for solid-oxide fuel cells, *Renew. Sustain. Energy Rev.* 51 (2015) 1–8, <https://doi.org/10.1016/j.rser.2015.05.069>.
- [52] G.H. Major, V. Fernandez, N. Fairley, E.F. Smith, M.R. Linford, Guide to XPS data analysis: applying appropriate constraints to synthetic peaks in XPS peak fitting, *J. Vac. Sci. Technol. A Vacuum, Surfaces, Film.* 40 (2022), 063201, <https://doi.org/10.1116/6.0001975>.
- [53] M.A. Peña, J.L.G. Fierro, Chemical structures and performance of perovskite oxides, *Chem. Rev.* 101 (2001) 1981–2017, <https://doi.org/10.1021/CR980129F/ASSET/IMAGES/LARGE/CR980129F00014.JPEG>.
- [54] S.P. Jiang, Development of lanthanum strontium cobalt ferrite perovskite electrodes of solid oxide fuel cells – a review, *Int. J. Hydrogen Energy* 44 (2019) 7448–7493, <https://doi.org/10.1016/j.ijhydene.2019.01.212>.
- [55] A. Nennung, A.K. Opitz, C. Rameshan, R. Rameshan, R. Blume, M. Hävecker, A. Knop-Gericke, G. Rupprechter, B. Klötzer, J. Fleig, Ambient pressure XPS study of mixed conducting perovskite-type SOFC cathode and anode materials under well-defined electrochemical polarization, *J. Phys. Chem. C* 120 (2016) 1461–1471, https://doi.org/10.1021/ACS.jpcc.5B08596/SUPPL_FILE/JP5B08596_SI_001.PDF.
- [56] Y. Bourlier, M. Frégnaux, B. Bérimi, A. Fouchet, Y. Dumont, D. Aureau, XPS monitoring of SrVO₃ thin films from demixing to air ageing: the asset of treatment in water, *Appl. Surf. Sci.* 553 (2021), 149536, <https://doi.org/10.1016/j.apusc.2021.149536>.
- [57] M. Siebenhofer, U. Haselmann, A. Nennung, G. Friedbacher, A.E. Bumberger, S. Wurster, W. Artner, H. Hutter, Z. Zhang, J. Fleig, M. Kubicek, Surface chemistry and degradation processes of dense La_{0.6}Sr_{0.4}CoO_{3-δ} thin film electrodes, *J. Electrochem. Soc.* 170 (2023), 014501, <https://doi.org/10.1149/1945-7111/ACADA8>.
- [58] Q. Gu, L. Wang, Y. Wang, X. Li, Effect of praseodymium substitution on La_{1-x}Pr_xMnO₃ (x=0–0.4) perovskites and catalytic activity for NO oxidation, *J. Phys. Chem. Solid.* 133 (2019) 52–58, <https://doi.org/10.1016/j.jpcs.2019.05.001>.

- [59] B. Kamecki, T. Miruszewski, J. Karczewski, Structural and electrical transport properties of Pr-doped SrTi_{0.93}Co_{0.07}O_{3-δ} a novel SOEC fuel electrode materials, *J. Electroceram.* 42 (2019) 31–40, <https://doi.org/10.1007/s10832-018-0143-0>.
- [60] M. Wang, J. Yang, B. Chi, J. Pu, J. Li, High performance Ni exsolved and Cu added La_{0.8}Ce_{0.2}Mn_{0.6}Ni_{0.4}O₃-based perovskites for ethanol steam reforming, *Int. J. Hydrogen Energy* 45 (2020) 16458–16468, <https://doi.org/10.1016/j.ijhydene.2020.04.108>.
- [61] E. Beyreuther, S. Grafström, L.M. Eng, C. Thiele, K. Dörr, XPS investigation of Mn valence in lanthanum manganite thin films under variation of oxygen content, *Phys. Rev. B* 73 (2006), 155425, <https://doi.org/10.1103/PhysRevB.73.155425>.
- [62] K. Kooser, T. Käämbre, M. Vestli, U. Joost, S. Urpelainen, M. Kook, F. Bournel, J. J. Gallet, E. Lust, E. Kukk, G. Nurk, Operando high-temperature near-ambient pressure X-ray photoelectron spectroscopy and impedance spectroscopy study of Ni–Ce_{0.9}Gd_{0.1}O_{2–δ} solid oxide fuel cell anode, *Int. J. Hydrogen Energy* 45 (2020) 25286–25298, <https://doi.org/10.1016/j.ijhydene.2020.06.228>.
- [63] H.P. Uppara, J.S. Pasupathy, S. Pradhan, S.K. Singh, N.K. Labhsetwar, H. Dasari, The comparative experimental investigations of SrMn(Co₃+Co₂)O_{3±δ} and SrMn(Cu₂+O₃)±δ perovskites towards soot oxidation activity, *Mol. Catal.* 482 (2020), <https://doi.org/10.1016/j.mcat.2019.110665>.
- [64] Y. Tu, S. Chen, X. Li, J. Gorbaciova, W.P. Gillin, S. Krause, J. Briscoe, Control of oxygen vacancies in ZnO nanorods by annealing and their influence on ZnO/PEDOT:PSS diode behaviour, *J. Mater. Chem. C* 6 (2018) 1815–1821, <https://doi.org/10.1039/c7tc04284a>.
- [65] P. Ding, W. Li, H. Zhao, C. Wu, L. Zhao, B. Dong, S. Wang, Review on Ruddlesden-Popper perovskites as cathode for solid oxide fuel cells, *J. Phys. Mater.* 4 (2021), <https://doi.org/10.1088/2515-7639/ABE392>.
- [66] Y. Wang, L. Yu, R. Wang, Y. Wang, X. Zhang, Reactivity of carbon spheres templated Ce/LaCo_{0.5}Cu_{0.5}O₃ in the microwave induced H₂O₂ catalytic degradation of salicylic acid: characterization, kinetic and mechanism studies, *J. Colloid Interface Sci.* 574 (2020) 74–86, <https://doi.org/10.1016/j.jcis.2020.04.042>.
- [67] C. Graves, C. Chatzichristodoulou, M.B. Mogensen, Kinetics of CO/CO₂ and H₂/H₂O reactions at Ni-based and ceria-based solid-oxide-cell electrodes, *Faraday Discuss* 182 (2015) 75–95, <https://doi.org/10.1039/C5FD00048C>.
- [68] L.J. van der Pauw, A method of measuring specific resistivity and HALL effect of discs of arbitrary shape, in: *Semicond. Devices Pioneer. Pap.*, WORLD SCIENTIFIC, 1991, pp. 174–182, https://doi.org/10.1142/9789814503464_0017.
- [69] J.B. Goodenough, Electronic and ionic transport properties and other physical aspects of perovskites, *Rep. Prog. Phys.* 67 (2004) 1915, <https://doi.org/10.1088/0034-4885/67/11/R01>.
- [70] F. Jin, Y. Shen, R. Wang, T. He, Double-perovskite PrBaCo₂/3Fe₂/3Cu₂/3O₅+δ as cathode material for intermediate-temperature solid-oxide fuel cells, *J. Power Sources* 234 (2013) 244–251, <https://doi.org/10.1016/j.jpowsour.2013.01.172>.
- [71] W. Xia, X. Liu, F. Jin, X. Jia, Y. Shen, J. Li, Evaluation of calcium codoping in double perovskite PrBaCo₂O₅+δ as cathode material for IT-SOFCs, *Electrochim. Acta* 364 (2020), <https://doi.org/10.1016/j.electacta.2020.137274>.
- [72] T. Ramos, M. Søgaard, M.B. Mogensen, Electrochemical characterization of Ni/ScYSZ electrodes as SOFC anodes, *J. Electrochem. Soc.* 161 (2014) F434–F444, <https://doi.org/10.1149/2.045404jes>.
- [73] C. Eндler-Schuck, J. Joos, C. Niedrig, A. Weber, E. Ivers-Tiffée, The chemical oxygen surface exchange and bulk diffusion coefficient determined by impedance spectroscopy of porous La_{0.58}Sr_{0.4}Co_{0.2}Fe_{0.8}O_{3–δ} (LSCF) cathodes, *Solid State Ionics* 269 (2015) 67–79, <https://doi.org/10.1016/j.ssi.2014.11.018>.
- [74] T. Ma, T. Xia, Q. Li, L. Sun, L. Huo, H. Zhao, Highly electrocatalytic activity Ruddlesden–Popper type electrode materials for solid oxide fuel cells, *J. Eur. Ceram. Soc.* 42 (2022) 490–498, <https://doi.org/10.1016/j.jeurceramsoc.2021.10.028>.
- [75] A. Nechache, M. Cassir, A. Ringué, Solid oxide electrolysis cell analysis by means of electrochemical impedance spectroscopy: a review, *J. Power Sources* 258 (2014) 164–181, <https://doi.org/10.1016/j.jpowsour.2014.01.110>.
- [76] M.K. Rath, K.T. Lee, Characterization of novel Ba₂LnMoO₆ (Ln = Pr and Nd) double perovskite as the anode material for hydrocarbon-fueled solid oxide fuel cells, *J. Alloys Compd.* 737 (2018) 152–159, <https://doi.org/10.1016/j.jallcom.2017.12.090>.
- [77] M.V. Sandoval, C. Cardenas, E. Capoen, P. Roussel, C. Pirovano, G.H. Gauthier, Performance of La_{0.5}Sr_{1.5}MnO_{4±δ} Ruddlesden-Popper manganite as electrode material for symmetrical solid oxide fuel cells. Part B. the hydrogen oxidation reaction, *Electrochim. Acta* 353 (2020), <https://doi.org/10.1016/j.electacta.2020.136494>.
- [78] B. Niu, F. Jin, L. Zhang, P. Shen, T. He, Performance of double perovskite symmetrical electrode materials Sr₂TiFe_{1–x}MoxO_{6–δ} (x = 0.1, 0.2) for solid oxide fuel cells, *Electrochim. Acta* 263 (2018) 217–227, <https://doi.org/10.1016/j.electacta.2018.01.062>.
- [79] F. Jin, L. Li, T. He, NdBaCo₂/3Fe₂/3Cu₂/3O₅+δ double perovskite as a novel cathode material for CeO₂- and LaGaO₃-based solid oxide fuel cells, *J. Power Sources* 273 (2015) 591–599, <https://doi.org/10.1016/j.jpowsour.2014.09.147>.
- [80] A. Nanning, M. Holzmann, J. Fleig, A.K. Opitz, Excellent kinetics of single-phase Gd-doped ceria fuel electrodes in solid oxide cells, *Mater. Adv.* 2 (2021) 5422–5431, <https://doi.org/10.1039/D1MA00202C>.
- [81] A. Atkinson, S.A. Baron, N.P. Brandon, AC impedance spectra arising from mixed ionic electronic solid electrolytes, *J. Electrochem. Soc.* 151 (2004) E186, <https://doi.org/10.1149/1.1690291/XML>.
- [82] B. He, L. Zhao, S. Song, T. Liu, F. Chen, C. Xia, Sr₂Fe_{1.5}Mo_{0.5}O_{6–δ}–Sm_{0.2}Ce_{0.8}O_{1.9} composite anodes for intermediate-temperature solid oxide fuel cells, *J. Electrochem. Soc.* 159 (2012) B619–B626, <https://doi.org/10.1149/2.020206jes>.
- [83] S. Wang, T. Kobayashi, M. Dokiya, T. Hashimoto, Electrical and ionic conductivity of Gd-doped ceria, *J. Electrochem. Soc.* 147 (2000) 3606, <https://doi.org/10.1149/1.1393946/XML>.
- [84] D.A. Osinkin, N.M. Bogdanovich, A.L. Gavrilyuk, Rate determining steps of fuel oxidation over CeO₂ impregnated Ni-YSZ in H₂ + H₂O + CO + CO₂ ambient, *Electrochim. Acta* 199 (2016) 108–115, <https://doi.org/10.1016/j.electacta.2016.03.133>.
- [85] W. Sitte, R. Merkle (Eds.), *High-Temperature Electrolysis*, IOP Publishing, 2023, <https://doi.org/10.1088/978-0-7503-3951-3>.
- [86] T. Zhu, D.E. Fowler, K.R. Poepelmeier, M. Han, S.A. Barnett, Hydrogen oxidation mechanisms on perovskite solid oxide fuel cell anodes, *J. Electrochem. Soc.* 163 (2016) F952–F961, <https://doi.org/10.1149/2.1321608JES/XML>.
- [87] V.M. Janardhanan, O. Deutschmann, Modeling of solid-oxide fuel cells, *Zeitschrift Fur Phys. Chemie* 221 (2007) 443–479, <https://doi.org/10.1524/ZPCH.2007.221.4.443/MACHINEREADABLECITATION/RIS>.
- [88] J. Nielsen, T. Klemens, P. Blennow, Detailed impedance characterization of a well performing and durable Ni:CGO infiltrated cermet anode for metal-supported solid oxide fuel cells, *J. Power Sources* 219 (2012) 305–316, <https://doi.org/10.1016/j.jpowsour.2012.07.031>.
- [89] L. Troncoso, J.A. Alonso, A. Aguadero, Low activation energies for interstitial oxygen conduction in the layered perovskites La_{1+x}Sr_{1–x}InO_{4+δ}, *J. Mater. Chem. A* 3 (2015) 17797–17803, <https://doi.org/10.1039/C5TA03185K>.
- [90] S.P. Jiang, W. Wang, Y.D. Zhen, Performance and electrode behaviour of nano-YSZ impregnated nickel anodes used in solid oxide fuel cells, *J. Power Sources* 147 (2005) 1–7, <https://doi.org/10.1016/j.jpowsour.2004.12.042>.
- [91] Q.X. Fu, F. Tietz, D. Stöver, La_{0.4}Sr_{0.6}Ti_{1–x}MnxO_{3–δ} perovskites as anode materials for solid oxide fuel cells, *J. Electrochem. Soc.* 153 (2006) D74, <https://doi.org/10.1149/1.2170585>.
- [92] S. Primdahl, M. Mogensen, Gas conversion impedance: a test geometry effect in characterization of solid oxide fuel cell anodes, *J. Electrochem. Soc.* 145 (1998) 2431–2438, <https://doi.org/10.1149/1.1838654>.
- [93] W.G. Bessler, S. Gewies, Gas concentration impedance of solid oxide fuel cell anodes, *J. Electrochem. Soc.* 154 (2007) B548, <https://doi.org/10.1149/1.2720639>.
- [94] Q.X. Fu, F. Tietz, D. Stöver, La_{0.4}Sr_{0.6}Ti_{1–x}MnxO_{3–δ} perovskites as anode materials for solid oxide fuel cells, *J. Electrochem. Soc.* 153 (2006) D74, <https://doi.org/10.1149/1.2170585>.
- [95] A. Atkinson, S.A. Baron, N.P. Brandon, AC impedance spectra arising from mixed ionic electronic solid electrolytes, *J. Electrochem. Soc.* 151 (2004) E186, <https://doi.org/10.1149/1.1690291/XML>.
- [96] J. Jamnik, J. Maier, Generalised equivalent circuits for mass and charge transport: chemical capacitance and its implications, *Phys. Chem. Chem. Phys.* 3 (2001) 1668–1678, <https://doi.org/10.1039/B100180L>.
- [97] W. Lai, S.M. Haile, Impedance spectroscopy as a tool for chemical and electrochemical analysis of mixed conductors: a case study of ceria, *J. Am. Ceram. Soc.* 88 (2005) 2979–2997, <https://doi.org/10.1111/J.1551-2916.2005.00740.X>.